Classical and quantal collisional Stark mixing at ultralow energies

D. Vrinceanu and M. R. Flannery
School of Physics, Georgia Institute of Technology, Atlanta, Georgia 30332
(Received 6 June 2000; published 2 February 2001)

Exact classical and quantal solutions are presented for the full array of intrashell transitions $n\ell \rightarrow n\ell'$, between any angular momentum states, induced by slow distant collisions with a charged particle. The collisions are adiabatic with respect to the orbital frequency of the atomic electron and the transitions are induced by the weak ion-atom dipole field generated by the ion moving along a classical path. The rich symmetry of the problem allows a unified approach and is the source of the excellent agreement, beyond the usual Ehrenfest's correspondence principle, between the classical and quantal treatments. A classical transition probability is defined. Probabilities for transition between any angular momentum states within a high Rydberg energy level are derived in exact analytic forms and are analyzed for a large number of numerical examples. The transition probabilities obtained from the three methods—quantal and classical formulations and Monte Carlo classical simulations—are directly compared to provide excellent agreement.

DOI: 10.1103/PhysRevA.63.032701 PACS number(s): 34.50.Pi, 34.60.+z, 34.10.+x

I. INTRODUCTION

The collision of a slow heavy charged particle with an excited atom at large impact parameters induces transitions between neighboring angular momentum states of the exited atom. For very low velocity of the projectile, the transitions with change in principal quantum number are much less probable than the quasielastic angular momentum changing collisions at large impact parameters. Because these states are very close in energy, or are even degenerate as for hydrogen and Rydberg atoms, the process is very efficient since little or no energy transfer is required. In fact, the cross sections increase as the energy of the incoming particle is decreased. This process is called Stark mixing and is important in many problems in atomic physics. For example, Bethe [1] analyzed the absorption of low-energy negative K^- mesons in liquid hydrogen on the recognition that the Stark mixing is essential in such processes. Also, Stark mixing is included in the calculation of the Auger (or autoionization) process, which follows the collision between ions and atoms [2] and in zero-electron-kinetic-energy (ZEKE) photoelectron spectroscopy [3]. Stark mixing has also been important in astrophysics (e.g., [4]), in recent efforts to produce antihydrogen at 4 K [5] and for general three-body recombination at ultralow energies [6]. The first stage in recombination at ultralow temperatures T_e [6] is a very rapid collisional capture into high Rydberg states with high angular momentum and large radiative lifetimes, at a rate proportional to $T_e^{-4.5}$. Since the n-changing collisions are relatively unimportant at ultralow energies, the ℓ-mixing collisions are essential in producing the low angular momentum states required to radiatively decay at relatively high rate to low n levels, thereby stabilizing the recombination.

Experiments [7] on single ion collisions with alkali-metal Rydberg atom have measured large ℓ-mixing cross sections for slow projectiles, including dipole-forbidden transitions. Various theoretical models have been developed to reproduce the experimental data. Even though a set of coupled-channel equations can be written, their solution becomes impractical for the large quantum numbers considered in the experiment ($n \approx 28$). On averaging over the azimuthal quantum number m, the size of the problem becomes much reduced and satisfactory results have been obtained [8]. Considering the Rydberg atom in a frame that rotates together with the internuclear axis, the Stark mixing problem is reduced to the problem of the Rydberg atom in mixed *static fields*: electric, provided by the projectile ion, and magnetic, produced by the noninertial (Coriolis) forces. In this way, the well known results (in both classical [9] and quantum [10,11] mechanics) for the problem of interaction between weak fields and an atom can be adopted [12] to provide a solution for the Stark mixing problem. In a remarkable series of papers, both classical [13–15] and quantal [15,16] versions of this approach have been successfully applied for the zero to higher angular momentum transitions, by including the quantum defect appropriate to the experiments [7]. Classical trajectory Monte Carlo simulations [17] were also in agreement with the experiments [7].

All theoretical efforts rely on the impact parameter formalism, in which the projectile is a classical particle moving along a definite trajectory. The dipole interaction has been proven to be a good approximation for the projectile-target potential because of the long-range Coulomb interactions and the decisive role of large impact parameters. For slow moving ions, Stark mixing can occur without energy transfer. The dynamics of the Rydberg atom is therefore adiabatic. The orbit of the Rydberg electron can still be considered elliptical, but its shape and orientation change slowly during the collision time, which is very much longer than the orbital time. This classical mechanics picture translates into the quantal description by restricting the dynamics to the energy shell, as prescribed by adiabatic perturbation theory.

In this paper, a unified theory for the general time-dependent solution of collisional Stark mixing is presented, both in the classical and quantal formulations. The exceptional rich dynamic symmetry of the hydrogen atom provides the key foundation that enables both the classical and quantal solutions to be constructed in a unified way (Sec. II) by using group representation theory. This classical-quantal correspondence transcends the well known Ehrenfest's theorem

(as observed in the general case of weak field-atom interaction [15,18]) just because of the SO(4) dynamical group symmetry[1] of the energy shell of the hydrogen atom. The agreement, as expected, is very good. It is shown that the present quantal solution (developed in Sec. III A) can be formulated (Sec. III B) so as to provide the rotating coordinate frame formal result obtained in [12,15,16]. The efficiency of the present quantal solution is demonstrated in Sec. VI. A new classical solution applicable to transitions between arbitrary angular momentum states is derived in Sec. IV A. We define the classical transition probability, in a language designed to exploit the dynamical symmetry, as the normalized volume of phase space accessible to both initial and final states in Sec. IV B. Monte Carlo simulations (Sec. V) are also performed to yield results in agreement with the classical expression for the Stark mixing probabilities.

II. KINEMATICS OF STARK MIXING

Stark mixing occurs when the electron of a Rydberg atom changes its angular momentum, without changing its energy, as a result of a collision, at large impact parameters, with a slow massive particle of charge Z_1e. In addition to the energy, given by the constant Hamiltonian

$$H_0=\frac{p^2}{2m_e}-\frac{e^2}{r},$$

the angular momentum $\mathbf{L}=\mathbf{r}\times\mathbf{p}$ of the unperturbed Rydberg electron and the Runge-Lenz (or eccentricity) vector

$$\mathbf{A}=\left[p^2\mathbf{r}-(\mathbf{p}\cdot\mathbf{r})\mathbf{p}-m_e e^2\frac{\mathbf{r}}{r}\right]\Big/\sqrt{-2m_eE}, \tag{1}$$

which is directed toward the pericenter and normalized to angular momentum units, are also conserved. These quantities define the dynamic SO(4) symmetry of the hydrogen atom with given energy E, which is a subgroup of the global SO(4,2) symmetry group. Because the SO(4) group is isomorphic with the direct product $SO(3)\oplus SO(3)$ of two rotation groups, a special decomposition

$$\mathbf{L}=\mathbf{M}+\mathbf{N},\quad \mathbf{A}=\mathbf{M}-\mathbf{N} \tag{2}$$

permits the dynamics of the hydrogen atom to be separated into two decoupled motions. The generators **M** and **N** act independently as angular momenta and are also conserved quantities for the unperturbed Rydberg atom. They evolve independently [9] with time on application of an electric field.

The orbital electron interacts with the time-dependent electric field $\vec{\mathcal{E}}(t)$ generated by the passing projectile of charge Z_1e. In the weak-field approximation, this field is constant over the spatial extent of the atom. In this approximation, which is the same as the dipole approximation, the interaction potential $V=e\vec{r}\cdot\vec{\mathcal{E}}$ is

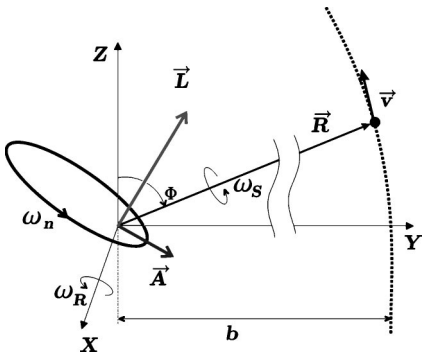

FIG. 1. Geometry of the Stark mixing collision.

$$V(\mathbf{r},\mathbf{R})=-Z_1e^2\frac{\mathbf{R}\cdot\mathbf{r}}{R^3}=\frac{Z_1e^2}{vb}\frac{d\Phi}{dt}\hat{R}\cdot\mathbf{r}$$

$$=\frac{Z_1e^2}{vb}\frac{d\Phi}{dt}(y\sin\Phi+z\cos\Phi). \tag{3}$$

The impact parameter b, the impact angle Φ, and internuclear vector **R** are displayed in Fig. 1. The angular momentum of relative motion $L_{\rm rel}=\mu R^2\dot{\Phi}=-\mu vb$ (where μ is the reduced mass of the projectile-target system) remains conserved since $L_{\rm rel}\gg L$ (so that $L_{\rm rel}$ and L are effectively decoupled).

Various frequencies or time scales are important to the present discussion of the collision, and are as follows.

(i) The projectile rotation (collision) frequency

$$\omega_R=-\frac{d\Phi}{dt}=\frac{bv}{R^2}\overset{\text{large } b}{\longrightarrow}\frac{v}{b}\approx\frac{1}{\tau_{coll}}$$

from which the collision time $\tau_{\rm coll}$ can be defined.

(ii) The transition frequency

$$\omega_{ij}=\frac{E_i-E_j}{\hbar}$$

of the Rydberg electron. For transitions $n\to n\pm1$ between neighboring levels, $\omega_{n,n\pm1}$ is simply $\omega_0/n^3=\omega_n=v_n/a_n$, the orbital frequency (the Bohr correspondence principle). Here $a_n=n^2a_0$ and $v_n=v_0/n$ are the averaged orbital radius and velocity.

(iii) The Stark precession frequency

$$\omega_S=\frac{3}{2}a_nv_n(\mathcal{E}/e)=\frac{3}{2}\frac{Z_1a_nv_n}{R^2}$$

for the precession of **A** about **R** provides the precessional frequency of the Runge-Lenz (eccentricity) vector **A** of the Rydberg orbit about the field direction $\hat{\mathcal{E}}$.

[1]This group contains sufficient generators to enable one to formulate the dynamics of the system solely in terms of operations of irreducible representations of the group [19].

(iv) The spin-orbit coupling frequency ω_{SO} corresponds with the maximum fine-structure splitting and is approximately [20] $\alpha_{FS}^2\omega_n/n$, where α_{FS} is the fine structure constant.

(v) The quantum defect frequency ω_{QD} is the precessional frequency of the electron orbit due to its interaction with the polarizable core. This frequency is important when one-electron atoms are considered other than hydrogen. The combined polarization of the core due to the orbital electron and the charged projectile has to be taken into account. Given the quantum defect δ_ℓ, the quantum defect frequency is

$$\omega_{QD} \approx 5\,\delta_\ell \omega_n/\ell$$

when ℓ is sufficiently large such that the core penetration and relativistic corrections can be ignored [21].

By considering the $\exp(i\omega t)$ factor in time-dependent perturbation theory, several types of collisions can be classified, as in [22], by comparing the above frequencies.

The Stark mixing parameter α is defined as the following ratio between the Stark and collision frequencies:

$$\alpha = \frac{\omega_S}{\omega_R} = \frac{3Z_1}{2}\left(\frac{a_n v_n}{bv}\right) = \frac{3Z_1}{2}\frac{\mu}{m_e}\frac{n\hbar}{L_{rel}}. \tag{4}$$

When $\alpha \ll 1$, then $\omega_S \tau_{coll} \ll 1$ and the collision time is much shorter than the Stark precessional time so that ℓ-changing or *Stark sudden* transitions are favored. This is in contrast to *Stark adiabatic* transitions where $\alpha \gg 1$; the electronic angular momentum does not change since the atom has sufficient time to relax to the Stark effect.

The orbital parameter β is the ratio

$$\beta = \omega_R/\omega_n = \frac{v}{v_n}\frac{a_n}{b} \equiv \frac{b_c}{b}.$$

For an *orbital adiabatic* collision, when $\beta \ll 1$ or $b \gg b_c$, the orbital electron adjusts itself adiabatically to the slow ion perturbation. Since $\omega_n \tau_{coll} \gg 1$, no energetic transitions occur. The *orbital sudden* regime, $\beta \gg 1$ or $b \ll b_c$, is associated with $\omega_n \tau_{coll} \ll 1$ and impulsive $n \to n'$ transitions.

The product of the α and β parameters defines the ratio $\omega_S/\omega_n = (3Z_1/2)(a_n/b)^2$, which depends only on b (and not v). For *weak fields* the Stark mixing splitting $\Delta E_S = \hbar\omega_S \ll \hbar\omega_n$, the $(n \to n \pm 1)$ energy gap. This also means that the internuclear distance R is much greater than the mean orbital radius a_n. In this approximation, the electron's orbital time is then much shorter than any characteristic collisional time to cause ℓ changes to the elliptical orbit. The vectors **A** and angular momentum **L**, which are constant for the unperturbed motion, then become good dynamical variables for the description of the perturbed motion, within the weak-field approximation.

With respect to orbital motion, the collision is sudden or adiabatic according to $b < b_C$ and $b > b_C$, respectively, where $b_C = (v/v_n)a_n$. With respect to the Stark frequency, the collision is adiabatic or sudden according to $b < b_S$ and $b > b_S$, respectively, where $b_S = (v_n/v)a_n$. The impact parameter b space can then be partitioned as in Fig. 2. As v decreases, b_S increases outward and b_C increases inward, thereby limiting the extent of the two sudden regions where n changes and ℓ mixing occurs. The variation with v can be represented by a (v,b) phase-space diagram partitioned into the characteristic regions as illustrated in Fig. 3. For $v > v^* = (3Z_1/2)^{1/2}v_n$, the (n,ℓ) changing and ℓ changing (orbital and Stark sudden) shaded regions overlap and expand, in direct contrast to ultracold speeds $v \leqslant v^*$, where the orbital and Stark adiabatic (clear) regions increase and the shaded regions diminish and do not overlap, thereby indicating few collisional changes. The region of interest here is the overlap of the orbital adiabatic $(\omega_R < \omega_n)$ region, $b > b_C = (v/v_n)a_n$, with the weak-field $(\omega_S < \omega_n)$ region, $b > b^* = (3Z_1/2)^{1/2}a_n$, i.e., the region in Fig. 3 defined by $b > b_C$ for $v \geqslant v^* = (3Z_1/2)^{1/2}v_n$ and by $b > b^*$ for $v \leqslant v^*$.

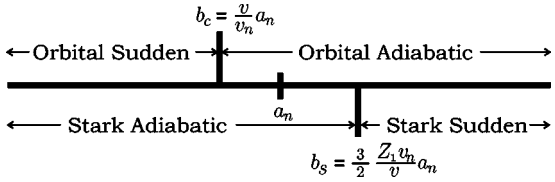

FIG. 2. Partitioning the impact parameter space b.

The following formulation assumes that the Rydberg atom, during the collision, occupies the same degenerate energy shell. The main element of the perturbation potential (3) is the electron position vector **r**, which by Pauli's replacement rule [23]

$$\mathbf{r} \approx \langle \mathbf{r} \rangle = -\frac{3}{2}\frac{\mathbf{A}}{p_n} \tag{5}$$

is replaced by its average $\langle \mathbf{r} \rangle$, a procedure valid for orbital adiabatic collisions (see Appendix A for a detailed explana-

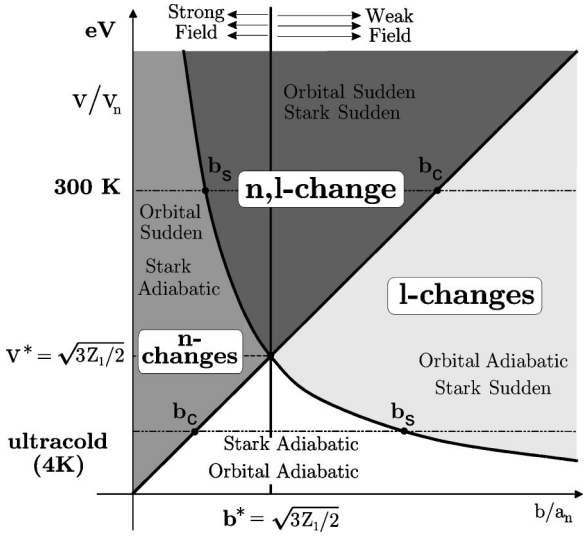

FIG. 3. Partitioning the v-b phase-space map into regions characterized mainly by (a) energy changes, (b) energy and angular momentum changes, (c) angular momentum changes, and (d) no changes. Regions for strong and weak field collisions are also shown.

tion). Since $Z_1e^2\mathbf{r}/bv$ is then $\alpha\mathbf{A}$, the perturbing potential (3) can be written in terms of the components A_2 and A_3 as

$$V(\alpha)=e\langle\vec{r}\rangle\cdot\vec{\mathcal{E}}(t)=-\alpha\frac{d\Phi}{dt}(A_2\sin\Phi+A_3\cos\Phi),$$

under the adiabatic, dipole and classical path assumptions. Moreover, the components $\{L_1,A_2,A_3\}$ generate a subgroup of the original symmetry group. The solution of the problem can then be written in terms of these symmetry-group generators and the Stark parameter α, which acts as a coupling constant. Under the above approximations, the collision parameters v, b, and Z_1 become combined into one parameter α.

The cross section for Stark mixing is

$$\sigma_{n\ell\to n\ell'}=2\pi\int_0^\infty P^{(n)}_{\ell'\ell}\,b\,db$$

$$=2\pi\left(\frac{3Z_1a_n}{2v/v_n}\right)^2\int_0^\infty P^{(n)}_{\ell'\ell}(\alpha,\Delta\Phi)\frac{d\alpha}{\alpha^3}. \qquad (6)$$

The probabilities $P^{(n)}_{\ell'\ell}$ obtained here are defined only in the full orbital adiabatic region $b>b_C$ for $v\geqslant v^*$ and in the adiabatic region restricted by the weak-field condition $b>b^*$ for $v\leqslant v^*$ (see Fig. 3). When $v<v^*$ and $b<b^*$, the Stark parameter $\alpha>1$. Since the transition probabilities are bounded for large α, the contribution to the α integration is vanishingly small for large α, decreasing as α^{-3}, and can be neglected for $\alpha>1$. Cross section (6) can then be defined at ultralow speeds $v\leqslant v^*$, when the *lower* limit b_{min} to the b-integration is taken as the weak-field limit b^*. For higher speeds $v>v^*$, the probabilities determined here are valid only in the full adiabatic region $b>b_C$ and do not hold in the (oribital sudden) region $b^*<b<b_C$ required in (6). In practical calculations of Eq. (6), various physical effects such as quantum defect, spin-orbit coupling, and Debye screening in a plasma determine an *upper* limit to the b integration and hence a lower limit α_{min} to the α integration. For example, the spin-orbit splitting overlaps with the Stark splitting when $b>b_{\max}$, where $b_{\max}\approx n^{5/2}\alpha_{\rm FS}^{-1}(3Z_1/2)^{1/2}a_0$. Similarly, the quantum defect comes into effect for the critical $b_{\max}\approx n^{5/2}\ell^{1/2}\delta_\ell^{-1/2}(3Z_1/10)^{1/2}a_0$. The Debye radius $R_D=(kT/4\pi^2Z_1e^2N)^{1/2}$, where T and N are the temperature and number density of the projectiles, is another viable upper limit to the impact parameter [4]. Stray electric fields in the collision region can also impose an upper limit to the impact parameter. The decision of which limit should be adopted in the definition (6) depends, of course, on the specific problem considered. These cutoff procedures are crucial for low angular momentum transfers where the transition probability $P(\alpha)$ cannot offset the $1/\alpha^3$ singularity (cf. Ref. [4]) as $b\to\infty$. The initial and final angles Φ_0 and Φ, between which the Stark mixing is effective, are also dependent on the specific cutoff procedure [14]. For trajectories with zero deflection ($\Delta\Phi=-\pi$), then Eq. (6) varies universally as $(Z_1a_n/v)^2$. Departure from this variation is governed by $\Delta\Phi(b,v)$ and by the physical limits imposed upon the α integration.

The discussion above is valid for both quantal and classical descriptions of Stark collisional mixing, since both involve only kinematics and general dynamical symmetry arguments. It is shown below (in Secs. III A and IV A) that both quantal and classical dynamics are governed by the following generic equation:

$$i\frac{\partial U}{\partial t}=\pm\alpha\frac{d\Phi}{dt}(J_2\sin\Phi+J_3\cos\Phi)U \qquad (7)$$

for the time evolution operator U within the rotation Lie group SO(3). The generators $\{J_1,J_2,J_3\}$ of this group have the commutators $[J_j,J_k]=i\epsilon_{jkn}J_n$, where ϵ_{jkn} is the Levi-Civita antisymmetric permutation symbol for any $j,k=1,2,3$. The required solution of Eq. (7) is

$$U(t,t_0)=e^{i\Phi J_1}\exp[-i\Delta\Phi(J_1\pm\alpha J_3)]e^{-i\Phi_0J_1}. \qquad (8)$$

This can be easily verified with the aid of the relations

$$e^{i\lambda J_2}J_1e^{-i\lambda J_2}=J_1\cos\lambda+J_3\sin\lambda,$$

$$e^{i\lambda J_2}J_3e^{-i\lambda J_2}=J_3\cos\lambda-J_1\sin\lambda,$$

$$e^{i\lambda J_1}J_3e^{-i\lambda J_1}=J_3\cos\lambda+J_2\sin\lambda,$$

which are derived from the basic identity

$$e^{\lambda A}Be^{-\lambda A}=B+\frac{\lambda}{1!}[A,B]+\frac{\lambda^2}{2!}[A,[A,B]]+\cdots \qquad (9)$$

and the above commutation relations. The net polar angle $\Delta\Phi$ swept during the collision between t_0 and t is $\Phi-\Phi_0$. The initial condition $U(t_0,t_0)=\mathbf{1}$ is automatically satisfied. If no cutoff radius is considered, $\Phi_0\to\pi$ as $t_0\to-\infty$ and $\Phi\to\Phi_D$ (the classical deflection angle) as $t\to\infty$. For the simplest case of distant straight line trajectories $\Phi_D=0$, and the evolution operator is then

$$U(\infty,-\infty)=\exp[i\pi(J_1\pm\alpha J_3)]e^{-i\pi J_1}$$

or, in terms of finite angle rotations $\mathcal{R}[\varphi,\mathbf{n}]$ by angle φ about direction $\mathbf{n}$ and the parameter $\gamma=\sqrt{1+\alpha^2}$, is

$$U(\infty,-\infty)=\mathcal{R}[-\gamma\pi,(1/\gamma,0,\pm\alpha/\gamma)]\mathcal{R}[\pi,(1,0,0)].$$

III. QUANTAL THEORY

A. Quantal intrashell dynamics

The Schrödinger equation for the time evolution operator $U(t,t_0)$ is

$$i\hbar\frac{\partial U}{\partial t}=(H_0+V)U, \qquad (10)$$

where H_0 is the free atom Hamiltonian and V is the interaction potential (3). If the projectile is moving sufficiently slowly, adiabatic perturbation theory can be applied and then

the whole dynamics of the target atom becomes restricted to the initial degenerate energy shell (the orbital adiabatic region in Fig. 3). This simple fact has two major consequences. First, the position operator and hence the perturbation potential (3) commute with the unperturbed Hamiltonian, as one can prove directly from the matrix elements of the commutator $[\mathbf{r},H_0]$ between any states within the energy E_n shell. The potential in the interaction representation

$$V_I = e^{iH_0 t/\hbar} V e^{-iH_0 t/\hbar}$$

is then identical with the potential in the Schrödinger representation ($V_I = V$), and the equation to be solved, in the interaction representation, is

$$i\hbar \frac{\partial U_I}{\partial t} = V U_I, \tag{11}$$

where $U_I(t,t_0) = \exp(iH_0 t/\hbar) U(t,t_0) \exp(-iH_0 t_0/\hbar)$. Second, the components x,y,z of the position operator do not commute between themselves when restricted to the energy shell. This follows from the well known Pauli ''replacement'' [23] $\mathbf{r} \to -3n\mathbf{A}/2$ (see Appendix A for details). This shows that the position vector $\mathbf{r}$ behaves, within the intrashell dynamics, like an angular momentum and is denoted by $\{\mathbf{r}\}$ when operating only within the n-shell. In fact, the set of operators $\{L_x, -2\{y\}p_n/3, -2\{z\}p_n/3\}$ generates a rotation group and Eqs. (11) and (7) are identical when $J_1 = L_x$, $J_2 = -2\{y\}p_n/3$ and $J_3 = -2\{z\}p_n/3$. Using the solution (8) of Eq. (7), the exact solution of Eq. (10) of Sec. II for the evolution operator, within the adiabatic approximation, is then

$$U_I(t,t_0) = e^{i\Phi L_1/\hbar} \exp\left[-\frac{i}{\hbar} \Delta\Phi \left(L_1 - \frac{2\alpha}{3} p_n \{z\} \right) \right] e^{-i\Phi_0 L_1/\hbar}. \tag{12}$$

This can also be directly verified by substituting Eq. (12) in Eq. (10) and using Eq. (9) with the appropriate commutator algebra.

The transition probability for a general $i \to f$ transition at time t is

$$a_{fi}(t) = \langle \Phi_f(\mathbf{r},t) | \Psi_i(\mathbf{r},t) \rangle \equiv \langle \Phi_f(\mathbf{r},t) | U(t,t_0) | \Psi_i(\mathbf{r},t_0) \rangle$$
$$= \langle \phi_f(\mathbf{r}) | U_I(t,t_0) | \phi_i(\mathbf{r}) \rangle,$$

where Ψ_i is the target wave function, which tends in the asymptotic limits ($t \to \pm\infty$) to the unperturbed basis set $\Phi_j(\mathbf{r},t) = \phi_j(\mathbf{r}) \exp(-iE_j t/\hbar)$. The transition amplitude for a Stark mixing process is

$$a^{(n)}_{\beta\alpha} = \langle n\beta | U_I(\infty,-\infty) | n\alpha \rangle, \tag{13}$$

where the initial state $i \equiv |n\alpha\rangle$ at $t = -\infty$ evolves to the final states $f \equiv |n\beta\rangle$ at $t = \infty$; α and β now label the states within the same energy shell. The superscript n will be omitted, since all dynamics is restricted to the energy shell described by quantum number n. When α and β label states with a given magnitude and projection of the angular momentum, the transition amplitude is given by Eq. (12) in Eq. (13) and is feasible and efficient for practical numerical applications.

The core of solution (12) is the exponential of the operator $L_1 - 2\alpha p_n z/3$. By using basic commutator algebra and Eq. (9), this operator is diagonalized as

$$e^{-iyq/\hbar} \left(L_1 - \frac{2\alpha}{3} p_n \{z\} \right) e^{iyq/\hbar} = \gamma L_1,$$

where $q = 2p_n \arctan(\alpha)/3$ and $\gamma = \sqrt{1+\alpha^2}$. The solution (12) has therefore the alternative form

$$U_I(t,t_0) = e^{i\Phi L_1/\hbar} e^{-i\{y\}q/\hbar} e^{-i\gamma\Delta\Phi L_1/\hbar} e^{i\{y\}q/\hbar} e^{-i\Phi_0 L_1/\hbar}, \tag{14}$$

which illustrates very effectively how the action of the slow distant encounter charged projectile coming from the negative z axis is decomposed into successive rotations about the x axis and alternating impulsive momentum transfers ($\pm q$) along the y axis.

It is interesting to compare the solution (14) obtained in this orbital adiabatic limit with the purely impulsive solution presented in sec. III C. The evolution operator (14), for undeflected collisions, yields

$$U_I(\infty,-\infty) = e^{-i\{y\}q/\hbar} e^{i\pi\gamma L_1/\hbar} e^{i\{y\}q/\hbar} e^{-i\pi L_1/\hbar}.$$

In the limit that $\alpha \to 0$, $q \to 2\alpha p_n/3 = \Delta q/2$ and $\exp(i\pi\gamma L_1/\hbar) \to \exp(i\pi L_1/\hbar)$. Then

$$U_I(\infty,-\infty)$$
$$= \left[1 + \frac{(-i)}{1!} \left(\frac{\{y\}\Delta q}{2\hbar} \right) + \frac{(-i)^2}{2!} \left(\frac{\{y\}\Delta q}{2\hbar} \right)^2 + \cdots \right] e^{i\pi L_1/\hbar}$$
$$\times \left[1 + \frac{i}{1!} \left(\frac{\{y\}\Delta q}{2\hbar} \right) + \frac{i^2}{2!} \left(\frac{\{y\}\Delta q}{2\hbar} \right)^2 + \cdots \right] e^{-i\pi L_1/\hbar},$$

which reduces, with the aid of $\exp(i\pi L_1/\hbar) y^n \exp(-i\pi L_1/\hbar) = y^n (\cos\pi)^n = (-y)^n$, to

$$U_I = e^{-2iq\{y\}/\hbar} + O(\alpha^2). \tag{15}$$

This limit merges with the impulsive result Eq. (20) below.

B. Formal development

It is interesting, however, to note that by introducing Pauli's replacement directly in the potential (3) and by writing the Runge-Lenz vector as $\mathbf{A} = \mathbf{M} - \mathbf{N}$, the potential decomposes as

$$V = V_M + V_N,$$

where

$$V_M = -\alpha (M_2 \sin\Phi + M_3 \cos\Phi) \dot{\Phi}$$

and

$$V_N = \alpha (N_2 \sin\Phi + N_3 \cos\Phi) \dot{\Phi}.$$

Because the commutators $[M_i,N_j] = 0$, $[M_i,H_0] = 0$, and $[N_i,H_0] = 0$ (for any $i,j = 1,2,3$ combination), the problem (10) becomes separable, exactly in the same way as the classical Stark mixing equations become decoupled (see the next section). The time evolution operator then factorizes as

TABLE I. The four bases useful for describing the quantal states of the hydrogen atom.

Basis	Quantum numbers	Complete set of commuting observable	Origin
orbital	$\|n\ell m\rangle_O$	H_0, L^2, L_3	Standard for spherical coordinates; describes correctly the states of the field-free atom
parabolic	$\|n_1 n_2 m\rangle_P$	H_1, H_2, L_3	Separation of Hamiltonian $H=H_1+H_2$ in parabolic coordinates, $\xi=r+z$, $\eta=r-z$, $\tan\varphi=y/x$; $n=n_1+n_2+\|m\|+1$
Stark	$\|nqm\rangle_S$	H_0, A_3, L_3	Parabolic basis; describes the Stark states for small electric field $\mathcal{E}$, when the interaction $-e\mathcal{E}z$ is diagonal; $q=n_1-n_2$
algebraic	$\|n\mu\nu\rangle_A$	H_0, M_3, N_3	The two rotation groups in which the dynamic symmetry group $SO(4)\equiv SO(3)\oplus SO(3)$ decomposes using Eq. (2); the equivalent angular momentum for both SO(3) representations is $j=(n-1)/2$; $\mu=(m+q)/2$ and $\nu=(m-q)/2$

$$U=U_{H_0}U_M U_N, \tag{16}$$

where, of course, $U_{H_0}=\exp[-iH_0(t-t_0)/\hbar]$, and U_M and U_N are the solutions of the equations $i\hbar\partial U_M/\partial t=V_M U_M$ and $i\hbar\partial U_N/\partial t=V_N U_N$, respectively. Using the group-theoretical result Eq. (8) of Sec. II, the solutions for the operators U_M and U_N are then

$$U_M=e^{i\Phi M_1/\hbar}\exp[-i/\hbar(\Phi-\Phi_0)(M_1-\alpha M_3)]e^{-i\Phi_0 M_1/\hbar} \tag{17}$$

and

$$U_N=e^{i\Phi N_1/\hbar}\exp[-i/\hbar(\Phi-\Phi_0)(N_1+\alpha N_3)]e^{-i\Phi_0 N_1/\hbar}. \tag{18}$$

In calculating the amplitude (13), four interesting basis sets can be chosen for the one electron hydrogenlike atom. Table I summarizes key properties of these bases. The orbital basis is useful for describing the field-free atom, before and after the collision, whereas the algebraic basis appears naturally as a basis where M_3 and N_3 are diagonal. The solution (16) has the simplest expression in this algebraic basis. All four bases in Table I span the n^2 degenerate energy shell and can be equally adopted to characterize the hydrogen atom. The algebraic basis spans a tensorial product of two spaces ($|\mu\rangle\otimes|\nu\rangle$) corresponding with spaces used for a matrix representation of the product $SO(3)\oplus SO(3)$. The two spaces have the same dimension because $M^2=N^2=(L^2+A^2)/4=(n^2-1)\hbar^2/4$ and are associated with two angular momenta with $j=(n-1)/2$.

The transition amplitude between the two algebraic states is then the product of two amplitudes for M and N independent actions, exactly in the same way in which the classical M and N vectors evolve independently in time, i.e., $a_{(\mu'\nu'),(\mu\nu)}=a_{\mu'\mu}a_{\nu'\nu}$. Each factor is the matrix element of a $j=(n-1)/2$ dimensional representation of the rotations represented by Eq. (16). For example, from Eq. (17), one gets $a_{\mu'\mu}=F_{\mu'\mu}(\alpha)$ with

$$F(\alpha)=\mathcal{D}^{(j)}\left[-\gamma\pi,\left(\frac{1}{\gamma},0,-\frac{\alpha}{\gamma}\right)\right]\mathcal{D}^{(j)}[\pi,(1,0,0)],$$

where $\mathcal{D}[\phi,(n_1,n_2,n_3)]$ is the Wigner matrix representation for the rotation $\mathcal{R}[\phi,\mathbf{n}]$ by angle ϕ about direction $\mathbf{n}$ (see [24] for the explicit expression). The transition probability in the space of $\mathbf{N}$ is the element $\nu'\nu$ of the matrix $F(-\alpha)$.

Calculation of the transition probability between orbital states requires the explicit unitary transformation between the orbital and algebraic bases. This can be obtained by direct scalar products of orbital and parabolic states for which explicit coordinate representations are known. The result can be written in terms of hypergeometric functions [25]. However, an equivalent result is provided by the $SO(4)\approx SO(3)\oplus SO(3)$ isomorphism. The orbital state, as a combination of two angular momentum states, is (see [26] for example)

$$|n\ell m\rangle=\sum_{\mu,\nu=-j}^{j}C_{\mu\nu}^{(\ell m)}|n\mu\nu\rangle,$$

where the transformation matrix $C^{(\ell m)}$ is given by the standard Clebsch-Gordan coefficients $\langle j\mu j\nu|\ell m\rangle$. The transition amplitude for the $\ell m\to\ell' m'$ transition is then

$$a_{\ell' m',\ell m}=\sum_{\mu\nu\mu'\nu'}C_{\mu'\nu'}^{(\ell' m')}C_{\mu\nu}^{(\ell m)}F_{\mu'\mu}(\alpha)F_{\nu'\nu}(-\alpha), \tag{19}$$

which can be expressed in matrix form as

$$a_{\ell' m',\ell m}=\mathrm{Tr}[C^{(\ell' m')}F(-\alpha)C^{(\ell m)T}F^T(\alpha)],$$

where C^T is the transpose of matrix C. The above result Eq. (19) is in exact agreement with the solution obtained in [12,15,16] using the rotating frame approach. The quantal development here in the fixed frame is exquisite in that it follows exactly the same reasoning basic to the exact classi-

cal mechanics solution (Sec. IV A). This result exhibits the essential power of the SO(4) symmetry group for the energy shell of the hydrogen atom. The common SO(4) symmetry therefore transcends the chosen formulation (classical or quantal) and provides a classical-quantal correspondence at a level more fundamental than Ehrenfest's theorem and the Heisenberg correspondence. In practice, the fourfold summation (19) and the use of the Wigner rotation matrices $\mathcal{D}$ for $F(\alpha)$ are not very efficient and the difficulty of calculation increases dramatically with n. Instead, the solution (12) provides a simpler approach, since the matrix elements of the argument in the exponential have simple expressions directly in the orbital basis. The array of transitions is obtained at once, within one matrix exponentiation of a band diagonal matrix for which efficient algorithms are available [27].

When the projection of the initial and final angular momentum is not determined, the transition probability is

$$P_{\ell'\ell}(\alpha)=\frac{1}{2\ell+1}\sum_{m=-\ell}^{\ell}\sum_{m'=-\ell'}^{\ell'}|a_{\ell' m',\ell m}|^2.$$

The exact quantal solution can therefore be derived directly without making use of unnecessary complications of a rotating frame and a fictitious magnetic field. The structure of the present solution Eq. (14) represents a sequence of alternating momentum transfers (in the y direction) and rotations about the x axis. This recognition motivates the following section.

C. Impulsive limit

In the other extreme situation (the orbital sudden–Stark sudden region in Fig. 3, where $\alpha\ll 1$), the impulsive limit, the collision is very fast and the collision time $\tau_{\rm coll}$ is much smaller than the orbital time. The potential has again the same form in both Schrödinger and interaction representations, $V=V_I$, since, in the equality $\langle f|V|i\rangle\equiv\langle f|V_I|i\rangle e^{i\omega_{fi}t}$, the exponent $\omega_{fi}t\ll 1$ [with $\omega_{fi}=(E_f-E_i)/\hbar$] can be replaced by zero. Now the position operator has **r** the normal behavior, in that its components commute between themselves. The impulsive transition amplitude is

$$a_{fi}^{\rm imp}=\langle\phi_f(\mathbf{r})|\exp-\frac{i}{\hbar}\int_{t_0}^{t}V(\mathbf{r},t')dt'|\phi_i(\mathbf{r})\rangle,$$

as may be directly verified upon using the closure relation. Since the force $\mathbf{F}=-\boldsymbol{\nabla}_{\mathbf{r}}V(\mathbf{r},t)$ acting on the Rydberg electron is impulsive and imparts momentum $\Delta\mathbf{q}$, then

$$\exp-\frac{i}{\hbar}\int_{t_0=-\infty}^{t=\infty}V(\mathbf{r},t')dt'=\exp-\frac{i}{\hbar}\int d\mathbf{r}\cdot\int_{-\infty}^{\infty}\mathbf{F}(\mathbf{r},t)dt$$
$$=\exp-\frac{i}{\hbar}\Delta\mathbf{q}\cdot\mathbf{r}$$

so that the probability amplitude for an impulsive collision is simply

$$a_{fi}^{\rm imp}(\mathbf{q})=\langle\phi_f|\exp-\frac{i}{\hbar}\Delta\mathbf{q}\cdot\mathbf{r}|\phi_i\rangle, \tag{20}$$

the inelastic form factor amplitude. This agrees with other alternative derivations [28,29] for the probability of an impulsive transition. The momentum transferred in an (impulsive) rectilinear collision is

$$\Delta\mathbf{q}=(2Z_1e^2/bv)\hat{y}=(4\alpha\hbar/3na_0)\hat{y}.$$

The transition amplitude, valid in the orbital and Stark sudden region (cf. Fig. 3), is therefore

$$a_{fi}^{\rm imp}(\alpha)=\langle\phi_f|\exp-i\frac{4}{3}\frac{\alpha}{n}\frac{y}{a_0}|\phi_i\rangle,$$

which connects with the $\alpha\to 0$ limit Eq. (15) of the adiabatic result Eq. (14). Even though this approximation is appropriate for the amplitude for transitions $n\ell\to n'\ell'$ between different energy shells, it is a good approximation, in particular for very small α [see Eq. (15)], if the normalized

$$\tilde{P}_{\beta\alpha}^{\rm imp}=|a_{\beta\alpha}^{\rm imp}|^2\Big/\sum_{\beta}|a_{\beta\alpha}^{\rm imp}|^2$$

transition probability is adopted for the problem of intrashell transitions. This normalization is a consequence of the difference between the operators $\{\mathbf{r}\}$, appropriate only to intrashell transitions, and **r** for all transitions.

IV. CLASSICAL THEORY

A. Classical intrashell dynamics

The angular momentum vector **L** and the Runge-Lenz vector defined by

$$\mathbf{A}=p_n^{-1}\left[\mathbf{p}\times\mathbf{L}-m_ee^2\frac{\mathbf{r}}{r}\right]$$

are constant for the unperturbed classical Rydberg atom. Moreover, $\mathbf{A}\cdot\mathbf{L}=0$ and $A^2+L^2=m_ea_n=n^2\hbar^2$. In the presence of an electric field of intensity $\vec{\mathcal{E}}$, the angular momentum **L** changes at the rate

$$\frac{d\mathbf{L}}{dt}=-e\vec{r}\times\vec{\mathcal{E}}.$$

On assuming that the collision is orbital adiabatic ($\dot{\Phi}\ll\omega_n$ and $\vec{\mathcal{E}}$ is constant over one period), the slow change of **L** during the collision is the classical average

$$\frac{\Delta\mathbf{L}}{T}=\left\langle\frac{d\mathbf{L}}{dt}\right\rangle_T=-\frac{e}{T}\int_{t-T/2}^{t+T/2}(\vec{r}\times\vec{\mathcal{E}})dt=-e\langle\vec{r}\rangle\times\vec{\mathcal{E}}(t)$$

over one orbital period T. Since the weak-field approximation ($\omega_S\ll\omega_n$) also holds, the vectors **L** and **A** then change very little over one orbital period. Using Pauli's replacement rule $\langle\mathbf{r}\rangle\approx-3\mathbf{A}/2p_n$, the following set of coupled equations can then be deduced [9,22]:

$$\frac{d\mathbf{A}}{dt} = -\omega_S \hat{\mathbf{R}} \times \mathbf{L}, \quad \frac{d\mathbf{L}}{dt} = -\omega_S \hat{\mathbf{R}} \times \mathbf{A},$$

where both $\omega_S = \alpha \dot{\Phi}$ and $\hat{R}$ vary with time. Under the substitution

$$\mathbf{M} = \frac{\mathbf{L}+\mathbf{A}}{2}, \quad \mathbf{N} = \frac{\mathbf{L}-\mathbf{A}}{2}, \tag{21}$$

the above set of differential equations becomes decoupled to yield

$$\frac{d\mathbf{M}}{dt} = -\omega_S \hat{\mathbf{R}} \times \mathbf{M}, \quad \frac{d\mathbf{N}}{dt} = +\omega_S \hat{\mathbf{R}} \times \mathbf{N}, \tag{22}$$

where the magnitudes $M^2 = N^2 = (L^2 + A^2)/4 = n^2\hbar^2/4$ remain constant throughout the collision. The classical analysis for constant electric fields is given by Born [9]. For time-independent ω_S, both **M** and **N** precess with constant frequency ω_S about the (fixed) direction of internuclear axis $\hat{R}$. For general time-varying ω_S, the system of differential equations (22) does not have an exact solution. Percival and Richards [22] have used classical perturbation theory to solve Eqs. (22) and then provided a diffusional theory of angular momentum mixing. Bellomo *et al.* [17] approached the same problem by proceeding via the time evolution propagator $U^{\pm}_{\rm rot}(t,t_0)$ for **M** and **N** in the rotating frame, an approach that results in formulas too complicated for physical changes $\Delta\mathbf{L}$ and $\Delta\mathbf{A}$ to be extracted. A special solution for transitions from angular momenta state $\ell = 0$ has been recently obtained by Kazansky and Ostrovsky [13–15].

An exact analytical solution is, however, possible under the weak field and orbital adiabatic approximations for a classical projectile trajectory and when the magnitude of vectors **M** and **N** remains constant during the collision, as for the present case of intrashell transitions. These vectors are then obtained at any moment by orthogonal transformations from the initial values $M(t_0)$ and $N(t_0)$. Let these transformations be $\tilde{U}_M(t,t_0)$ and $\tilde{U}_N(t,t_0)$, respectively. Then $\mathbf{M}(t) = \tilde{U}_M(t,t_0)\mathbf{M}(t_0)$ and a similar equation holds for the time evolution of **N**. The first equation in Eq. (22) becomes

$$\frac{d\tilde{U}_{ij}}{d\Phi} = -\alpha \epsilon_{ink} \hat{R}_n \tilde{U}_{kj},$$

where ϵ_{ijk} is the fully antisymmetric permutation symbol. Because the infinitesimal generators $\tilde{J}_k$ for the rotation group are matrices with elements $(\tilde{J}_k)_{ij} = -\epsilon_{ijk}$ (see [30] for example) and since $\hat{R} = (0, \sin\Phi, \cos\Phi)$, the above equation in matrix form is

$$\frac{d\tilde{U}_M}{d\Phi} = -\alpha(\sin\Phi \tilde{J}_2 + \cos\Phi \tilde{J}_3)\tilde{U}_M,$$

where $[\tilde{J}_k, \tilde{J}_j] = \epsilon_{kjn}\tilde{J}_n$. This equation is the matrix representation of the group equation (7) and the solution $\tilde{U}_M$ is the matrix representation of the general solution (8). The final vector $\mathbf{M}'$ is therefore obtained from the initial vector **M** by three successive rotations,

$$\mathbf{M}' = \mathcal{R}[-\Phi,(1,0,0)]\mathcal{R}[\gamma\Delta\Phi,(1/\gamma,0,-\alpha/\gamma)] \times \mathcal{R}[\Phi_0,(1,0,0)]\mathbf{M}. \tag{23}$$

The solution for **N** has the similar form

$$\mathbf{N}' = \mathcal{R}[-\Phi,(1,0,0)]\mathcal{R}[\gamma\Delta\Phi,(1/\gamma,0,+\alpha/\gamma)] \times \mathcal{R}[\Phi_0,(1,0,0)]\mathbf{N} \tag{24}$$

obtained simply by replacing α by $-\alpha$ in the corresponding equation for **M**. The matrix $\mathcal{R}[\Phi,\mathbf{n}]$ is the rotation matrix for a vector and corresponds with the representation of the abstract rotation (specified by the angle Φ and the direction **n** of rotation) on the three-dimensional vector space. Analytical expression for U_M and U_N can be obtained [31] as explicit functions of α and $\Delta\Phi$. In particular, when $\Phi = 0$ and $\Phi_0 = \pi$, the (3×3) matrix $\tilde{U}_M$ is

$$\tilde{U}_M = \begin{bmatrix} \gamma^{-2}[1+\alpha^2\cos(\pi\gamma)] & \alpha\gamma^{-1}\sin(\pi\gamma) & \alpha\gamma^{-2}[1-\cos(\pi\gamma)] \\ \alpha\gamma^{-1}\sin(\pi\gamma) & -\cos(\pi\gamma) & -\gamma^{-1}\sin(\pi\gamma) \\ \alpha\gamma^{-2}[\cos(\pi\gamma)-1] & \gamma^{-1}\sin(\pi\gamma) & -\gamma^{-2}[\alpha^2+\cos(\pi\gamma)] \end{bmatrix} \tag{25}$$

and $\tilde{U}_N$ is obtained from $\tilde{U}_M$ by replacing α with $-\alpha$.

As a result of the collision, the initial state of the target atom, specified by the vectors $(\mathbf{L},\mathbf{A})$, changes to the final state $(\mathbf{L}',\mathbf{A}')$ according to

$$\mathbf{L}' = \frac{\tilde{U}_M+\tilde{U}_N}{2}\mathbf{L} + \frac{\tilde{U}_M-\tilde{U}_N}{2}\mathbf{A}, \tag{26}$$

$$\mathbf{A}' = \frac{\tilde{U}_M-\tilde{U}_N}{2}\mathbf{L} + \frac{\tilde{U}_M+\tilde{U}_N}{2}\mathbf{A}. \tag{27}$$

For the undeflected trajectory of the projectile, when $\Phi = 0$ and $\Phi_0 = \pi$, explicit results are:

$$
\begin{aligned}
L_1' &= \gamma^{-2}[1+\alpha^2\cos(\pi\gamma)]L_1 + \alpha\gamma^{-1}\sin(\pi\gamma)A_2 + \alpha\gamma^{-2}[1-\cos(\pi\gamma)]A_3,\\
L_2' &= -\cos(\pi\gamma)L_2 - \gamma^{-1}\sin(\pi\gamma)L_3 + \alpha\gamma^{-1}\sin(\pi\gamma)A_1,\\
L_3' &= \gamma^{-1}\sin(\pi\gamma)L_2 - \gamma^{-2}[\alpha^2+\cos(\pi\gamma)]L_3 + \alpha\gamma^{-2}[\cos(\pi\gamma)-1]A_1,\\
A_1' &= \gamma^{-2}[1+\alpha^2\cos(\pi\gamma)]A_1 + \alpha\gamma^{-1}\sin(\pi\gamma)L_2 + \alpha\gamma^{-2}[1-\cos(\pi\gamma)]L_3,\\
A_2' &= -\cos(\pi\gamma)A_2 - \gamma^{-1}\sin(\pi\gamma)A_3 + \alpha\gamma^{-1}\sin(\pi\gamma)L_1,\\
A_3' &= \gamma^{-1}\sin(\pi\gamma)A_2 - \gamma^{-2}[\alpha^2+\cos(\pi\gamma)]A_3 + \alpha\gamma^{-2}[\cos(\pi\gamma)-1]L_1.
\end{aligned}
\tag{28}
$$

Here $\gamma=\sqrt{1+\alpha^2}$ and the components of the initial and final vectors are defined in the fixed coordinate frame of Fig. 1. Similar expressions have also been obtained [31] for general $\Delta\Phi$. The above exact solutions are easily verified and satisfy the invariant relations

$$\mathbf{L}'\cdot\mathbf{A}'=\mathbf{L}\cdot\mathbf{A}=\mathbf{0}$$

and

$$\mathbf{L}'^2+\mathbf{A}'^2=\mathbf{L}^2+\mathbf{A}^2=n^2\hbar^2.$$

The orbit of the final state $(n,\mathbf{L}')$ is confined to a plane perpendicular to the final $\mathbf{L}'$ and the energy is preserved (n is not changed).

B. Classical transition probability

The initial state is defined by the angular momentum **L** and Runge-Lenz **A** vectors. Apart from the constraints that (i) the magnitude of the **L** vector is $\ell\hbar$, (ii) the magnitude of the **A** vector is $\hbar\sqrt{n^2-\ell^2}$ in the given state, and (iii) **L** and **A** are always orthogonal, the two vectors are completely random in the six-dimensional space $\{\mathbf{L}\}\otimes\{\mathbf{A}\}$, which is a mapping of the usual $(\mathbf{r},\mathbf{p})$ phase space. The initial angular momentum can have any value between 0 and $n\hbar$. The special case of zero initial angular momentum requires a separate analysis, presented at the end of this section. In the following discussion, the initial angular momentum is assumed strictly positive.

The hypersurface in the $\{\mathbf{L}\}\otimes\{\mathbf{A}\}$ space on which the initial state is uniformly distributed is restricted by the above constraints and has the volume

$$\mathcal{V}_{n\ell}=\int\int \delta(|\mathbf{L}|-\hbar\ell)\,\delta(|\mathbf{A}|-\hbar\sqrt{n^2-\ell^2})\,\delta(\mathbf{L}\cdot\mathbf{A})\,d\mathbf{L}\,d\mathbf{A}, \tag{29}$$

which, upon integration, reduces to

$$\mathcal{V}_{n\ell}=8\pi^2\hbar^2\ell\sqrt{n^2-\ell^2}.$$

Each point within this manifold evolves during the collision according to the rules (28), so that only a fraction of possible initial states can have the final angular momentum ℓ' after the collision. Following the definition (29), the overlap volume of accessible $(\mathbf{L},\mathbf{A})$ space that contains both initial and final states is

$$\mathcal{V}_{n\ell\ell'}=\int\int \delta(|\mathbf{L}|-\ell\hbar)\,\delta(|\mathbf{L}'|-\ell'\hbar)\,\delta(|\mathbf{A}|-\hbar\sqrt{n^2-\ell^2}) \times\delta(\mathbf{L}\cdot\mathbf{A})\,d\mathbf{L}\,d\mathbf{A}. \tag{30}$$

The transition probability is then, in a geometric sense, the ratio of two volumes: the volume $\mathcal{V}_{n\ell\ell'}$ of the accessible states compatible with the required final angular momentum and the volume of the acceptable initial states $\mathcal{V}_{n\ell}$. The $\ell\rightarrow\ell'$ transition probability is therefore defined as the ratio

$$P^{(n)}_{\ell'\ell}=\frac{\mathcal{V}_{n\ell\ell'}}{\mathcal{V}_{n\ell}} \tag{31}$$

of phase-space volumes. Transformation to the alternative set of vectors **M** and **N** defined by Eq. (2) facilitates evaluation of the integral (30). The Jacobian of this transformation is $d\mathbf{L}\,d\mathbf{A}=8\,d\mathbf{M}\,d\mathbf{N}$. With the aid of the identities

$$\delta(\mathbf{L}\cdot\mathbf{A})=\delta(M^2-N^2)=\delta(N-M)/2M,$$

$$
\begin{aligned}
\delta(|\mathbf{L}|-\ell\hbar) &= \delta(\sqrt{2M^2(1+\cos\angle\mathrm{MN})}-\ell\hbar)\\
&= \delta(\cos\angle\mathrm{MN}-(\ell^2\hbar^2/2M^2-1))\ell\hbar/M^2,
\end{aligned}
$$

$$
\begin{aligned}
\delta(|\mathbf{A}|-\hbar\sqrt{n^2-\ell^2}) &= \delta(\sqrt{2M^2(1-\cos\angle\mathrm{MN})}-\hbar\sqrt{n^2-\ell^2})\\
&= \delta(\sqrt{4M^2-\ell^2\hbar^2}-\hbar\sqrt{n^2-\ell^2})\\
&= \delta(M-n\hbar/2)\hbar\sqrt{n^2-\ell^2}/4M,
\end{aligned}
$$

$$
\begin{aligned}
\delta(|\mathbf{L}'|-\ell'\hbar) &= \delta(\sqrt{2M^2(1+\cos\angle\mathrm{M'N'})}-\ell'\hbar)\\
&= \delta(\cos\angle\mathrm{M'N'}-(\ell'^2\hbar^2/2M^2-1))\ell'\hbar/M^2,
\end{aligned}
$$

the accessible phase-space volume is

$$\mathcal{V}_{n\ell\ell'}=\int\int 8M^2N^2\,d\Omega_M\,d\Omega_N d\,M\,dN$$
$$\times\frac{\delta(N-M)}{2M}\hbar\,\frac{\sqrt{n^2-l^2}}{4M}\,\delta(M-n\hbar/2)\frac{\ell\hbar}{M^2}$$
$$\times\delta\left[\cos\angle\mathrm{MN}-\left(\frac{\ell^2\hbar^2}{2M^2}-1\right)\right]\frac{\ell'\hbar}{M^2}$$
$$\times\delta\left[\cos\angle\mathrm{M'N'}-\left(\frac{\ell'^2\hbar^2}{2M^2}-1\right)\right].$$

This finally reduces to the simpler form

$$\mathcal{V}_{n\ell\ell'}=\frac{\sqrt{n^2-\ell^2}}{n^2}4\ell\ell'\hbar\int\int d\Omega_M\,d\Omega_N$$
$$\times\delta(\cos\angle\mathrm{MN}-\beta)\,\delta(\cos\angle\mathrm{M'N'}-\beta'),$$

where the integral is now over only the angular part of the vectors **M** and **N** and where the parameters β and β' are simply related to the initial and final states by

$$\beta=\frac{2\ell^2}{n^2}-1,\quad \beta'=\frac{2\ell'^2}{n^2}-1. \tag{32}$$

The final vectors $\mathbf{M}'=\tilde{U}_M\mathbf{M}$ and $\mathbf{N}'=\tilde{U}_N\mathbf{N}$ are given by finite rotation [Eqs. (23) and (24)] of the initial **M** and **N**, so that the relative angles $\angle\mathrm{MN}$ and $\angle\mathrm{M'N'}$ are independent of the specific coordinate frame chosen. Then

$$\cos\angle\mathrm{M'N'}=\frac{\mathbf{M}'\cdot\mathbf{N}'}{M^2}=\frac{(\tilde{U}_M\mathbf{M})\cdot(\tilde{U}_N\mathbf{N})}{M^2}$$
$$=\frac{(\tilde{U}_N^T\tilde{U}_M\mathbf{M})\cdot\mathbf{N}}{M^2}=\cos\angle\mathrm{M''N},$$

where $\mathbf{M}''$ is obtained by rotation from **M** using the operator $\tilde{U}_N^T\tilde{U}_M$. Being a product of two rotations, this operator is also a rotation about some direction $\boldsymbol{\nu}$ by the angle χ determined from the trace

$$\mathrm{Tr}[\tilde{U}_N^T\tilde{U}_M]=1+2\cos\chi$$

of the rotation operator. The proper rotation angle χ depends only on the collision (Stark) parameter α and the polar angle $\Delta\Phi=\Phi-\Phi_0$ swept out during collision time interval (t_0,t) and is independent of the initial or the final state of the Kepler atom. It is determined by

$$\cos\frac{\chi}{2}=[1+\alpha^2\cos(\sqrt{1+\alpha^2}\Delta\Phi)]/(1+\alpha^2).$$

For small $\alpha\ll1$, $\cos\chi\approx1-8\alpha^2\sin^2(\Delta\Phi/2)+O(\alpha^3)$ so that $\chi\approx4\alpha\sin(\Delta\Phi/2)+O(\alpha^3)$. The plot Fig. 4 of the ''universal'' function $\chi(\alpha,\Delta\Phi)$ for the case $\Delta\Phi=-\pi$ shows that χ has a maximum at $\alpha\approx0.9$ and is never greater than π. When

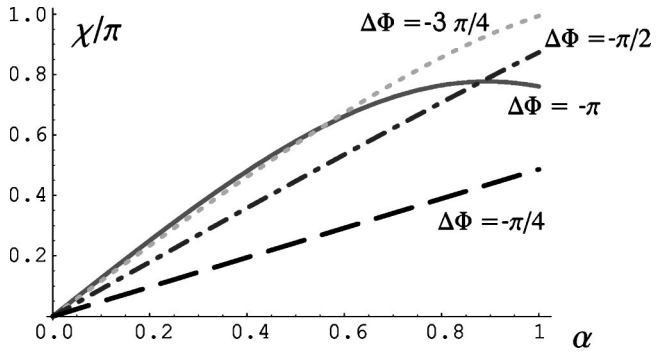

FIG. 4. The proper rotation angle χ as a function of the Stark parameter α for the net polar angle swept $\Delta\Phi=-\pi$, $-3\pi/4$, $-\pi/2$, and $-\pi/4$.

$\Delta\Phi\approx-3\pi/4$, the angle χ increases up to π as α increases to unity. For smaller values of $\Delta\Phi$, the angle χ increases monotonically with α.

The classical transition probability (31) is then

$$P^{(n)}_{\ell'\ell}=\frac{\ell'}{2\pi^2\hbar n^2}\int\int d\Omega_M\,d\Omega_N$$
$$\times\delta(\cos\angle\mathrm{MN}-\beta)\,\delta(\cos\angle\mathrm{M''N}-\beta'),$$

where the angle between **M** and $\mathbf{M}''$ is χ. The $d\Omega_N$ integral can be done first if one chooses to work in spherical coordinates with the z axis along the vector $\boldsymbol{\nu}$. In doing this, the vectors **M** and $\mathbf{M}''$ are fixed and have the coordinates $(\Theta,0)$ and (Θ,χ) as depicted in Fig. 5. The surface area element is $d\Omega_N=d(\cos\theta)d\phi$, where θ and ϕ are the spherical coordinates of the vector **N**. Instead of the (θ,ϕ) system, a new set of coordinates can be defined by (u_1,u_2), the angles of **N** with **M** and, respectively, $\mathbf{M}''$. The surface area element is now $d\Omega_N=du_1du_2/\sin\Delta$, where Δ is the angle between the NM and NM'' arcs, as in Fig. 5. A proof of this result is derived in Appendix B.

The $d\Omega_N$ integral is now simpler to evaluate and yields

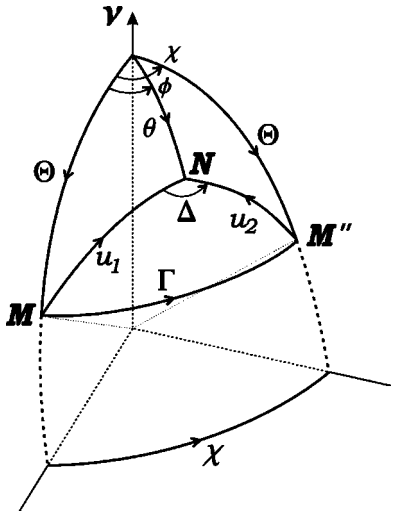

FIG. 5. The geometry and coordinates used in solving the integral (31).

$$P^{(n)}_{\ell'\ell}=\frac{2\ell'}{\pi\hbar n^2}\int_{-1}^{1} d(\cos\Theta)(\sin\Delta\sin u_1\sin u_2)^{-1},$$

where $\cos u_1=2\ell^2/n^2-1$, $\cos u_2=2\ell'^2/n^2-1$, and the factor 2 arises because the $(\theta,\ \phi)\rightarrow(u_1,u_2)$ transformation is not single-valued.

Basic trigonometry (see [32]) applied to spherical triangle **MNM**″ yields

$$\cos\Gamma=\cos u_1\cos u_2+\sin u_1\sin u_2\cos\Delta$$

so that

$$\sin u_1\sin u_2\cos\Delta=(\cos\Gamma_- -\cos\Gamma)(\cos\Gamma-\cos\Gamma_+),$$

where $\Gamma_\pm=u_1\pm u_2$ are the limits to Γ as Δ rotates through 2π. Since

$$\cos\Gamma=\cos\Theta^2+\sin\Theta^2\cos\chi$$

for spherical triangle $\mathbf{M}\nu\mathbf{M}''$, then

$$\sin u_1\sin u_2\sin\Delta=(1-\cos\chi)[(\cos^2\Theta-\mathcal{A})\times(\mathcal{B}-\cos^2\Theta)]^{1/2},$$

where

$$\mathcal{A}(\ell/n,\ell'/n;\alpha)=\frac{\cos(u_1+u_2)-\cos\chi}{1-\cos\chi},$$

$$\mathcal{B}(\ell/n,\ell'/n;\alpha)=\frac{\cos(u_1-u_2)-\cos\chi}{1-\cos\chi}. \tag{33}$$

On denoting $\cos\Theta$ by z, the transition probability is the one-dimensional integral

$$P^{(n)}_{\ell'\ell}(\chi)=\frac{2\ell'}{\pi\hbar n^2}\frac{1}{1-\cos\chi}\int\frac{dz}{\sqrt{(z^2-\mathcal{A})(\mathcal{B}-z^2)}},$$

where the limits of integration are defined by the condition of reality for the square-root function. The last integral can now be expressed in terms of the complete elliptic integral $K(m)=\int_0^{\pi/2}(1-m\sin^2x)^{-1/2}dx$ so that

$$P^{(n)}_{\ell'\ell}(\chi)=\frac{2\ell'}{\pi\hbar n^2}\frac{1}{\sin^2\chi/2}\begin{cases}0 & \text{if}\quad \mathcal{B}<0\\ K\left(\dfrac{\mathcal{B}}{\mathcal{B}-\mathcal{A}}\right)\Big/\sqrt{\mathcal{B}-\mathcal{A}} & \text{if}\quad \mathcal{B}>0,\quad \mathcal{A}<0\\ K\left(\dfrac{\mathcal{B}-\mathcal{A}}{\mathcal{B}}\right)\Big/\sqrt{\mathcal{B}} & \text{if}\quad \mathcal{B}>0,\quad \mathcal{A}>0\end{cases} \tag{34}$$

provides the exact classical probability as a function of ℓ, ℓ', and $\sin^2\chi/2$, which combines the Stark parameter $\alpha=(3Z_1/2)(a_nv_n/bv)$ and the net polar angle swept during the collision $\Delta\Phi$ into one function. The probability (34) satisfies detailed balance $2\ell P_{\ell'\ell}=2\ell' P_{\ell\ell'}$, where 2ℓ is the classical weight of the state $n\ell$.

Inspecting the definitions (33) reveals more qualitative aspects. First, $\mathcal{A}$ and $\mathcal{B}$ are always less than 1, and only $\mathcal{B}$ can attain 1 when $u_1=u_2$, i.e., for elastic collisions $\ell=\ell'$. The transition probability reduces, for this case, to the simpler form

$$P^{(n)}_{\ell\ell}(\alpha\rightarrow0)\approx\frac{1}{4\alpha\sqrt{n^2-\ell^2}}$$

in the limit of small α, thereby exhibiting the $1/\alpha$ singularity of elastic transitions. For transitions with $\ell'\neq\ell$ and small enough α, the factor $\mathcal{B}$ is negative and then the transition probability is zero. $\mathcal{B}$ is always greater than $\mathcal{A}$ because $\cos(u_1-u_2)\geqslant\cos(u_1+u_2)$. In the limit of each ℓ and $\ell'\rightarrow0$ or n, then $u_{1,2}=0$ or π and $\mathcal{A}=\mathcal{B}<1$. For $\ell\rightarrow\ell'=0$ transitions, the probability is zero. For the important case of zero initial angular momentum, the transition probability P in the limit of $\ell\rightarrow0$ is

$$P^{(n)}_{\ell'0}(\alpha)=\frac{\ell'/(\hbar n^2)}{\sin(\chi/2)\sqrt{\sin^2(\chi/2)-(\ell'/n)^2}}. \tag{35}$$

This result was also obtained in [14]. When $\ell'=n$, the transition probability is

$$P^{(n)}_{n\ell}(\alpha)=\frac{1/(\hbar n)}{\sin(\chi/2)\sqrt{(\ell/n)^2-\sin^2(\chi/2)}}.$$

When the argument of the square-root function is negative, the transition probability is zero. Similarly, for maximum initial angular momentum $\ell=n$, the transition probability has the limit

$$P^{(n)}_{\ell'n}(\alpha)=\frac{\ell'/(\hbar n^2)}{\sin(\chi/2)\sqrt{(\ell'/n)^2-\sin^2(\chi/2)}},$$

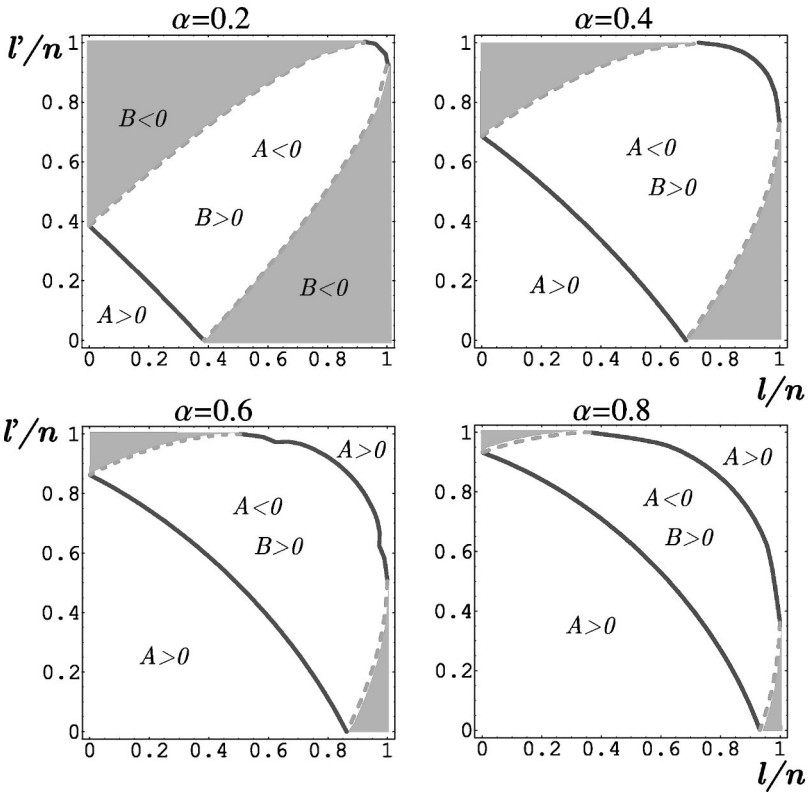

FIG. 6. Contour plots of the solutions of $\mathcal{A}=0$ (solid line) and $\mathcal{B}=0$ (dotted line) for various values of α. In gray zones $\mathcal{B}<0$ and the transition is classically forbidden.

where, again, the transition probability is zero unless the final angular momentum ℓ' is large enough to make the argument of the square-root function positive. If $\mathcal{B}>0$ and $\mathcal{A}$ is small, the transition probability has a singularity, typical for classical mechanics. Because the complete elliptic K function diverges logarithmically when the argument is very close to unity, the transition probability has the following expansion for small $\mathcal{A}$:

$$P \approx \frac{1}{\sqrt{\mathcal{B}}}(2\ln 2 - \tfrac{1}{2}\ln \mathcal{A}/\mathcal{B}).$$

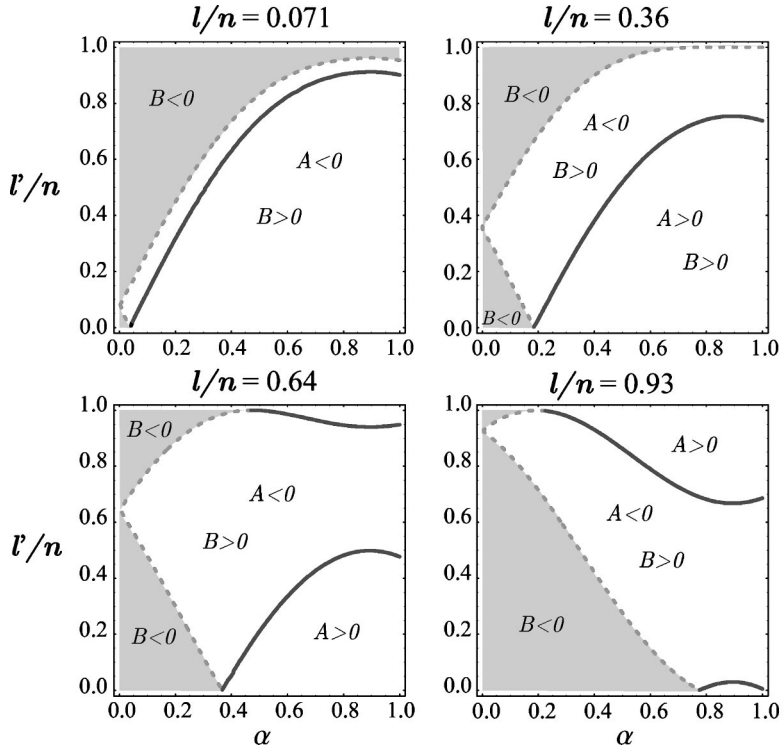

FIG. 7. Contour plots of the solutions of $\mathcal{A}=0$ (solid line) and $\mathcal{B}=0$ (dotted line) for various values of ℓ. In gray zones $\mathcal{B}<0$ and the transition is classically forbidden.

When $\mathcal{B}$ has small but positive values, the transition probability has a finite limit because $K(0)=\pi/2$. Of course, when $\mathcal{B}$ approaches zero from negative values, the transition probability is zero. Thus, the singularities in the transition probability are given by the solutions of the equations $\mathcal{A}=0$ and $\mathcal{B}=0$, which are $u_2=\pm u_1\pm\chi$.

A map of the various zones in the plane of reduced initial and final angular momenta $(\ell/n,\ell'/n)$ is displayed in Fig. 6 for the four values $\alpha=0.2$, 0.4, 0.6, and 0.8 of the Stark parameter. In the central region, $\mathcal{A}$ is negative and $\mathcal{B}$ is positive. Within the lower left and upper right corners, both $\mathcal{B}$ and $\mathcal{A}$ are positive. The transition is classically forbidden in the upper left and lower right corners (gray zones) where $\mathcal{B}<0$. Along the solid line, $\mathcal{A}=0$ lines, which represent $\cos^{-1}(\ell/n)+\cos^{-1}(\ell'/n)=\chi/2,\pi/2-\chi$, the transition probability has a logarithmic (cusp) singularity. Across the dotted $\mathcal{B}=0$ lines, which represent $\cos^{-1}(\ell/n)-\cos^{-1}(\ell'/n)=\chi/2,\pi-\chi/2$, the transition probability jumps from zero (in the gray zone) to some finite value (in the central zone). As $\alpha\to0$, the two inaccessible regions (where $\mathcal{B}<0$) increase until the central region with $\mathcal{B}>0$ and $\mathcal{A}<0$ becomes an elongated line strip lying along the diagonal $\ell=\ell'$. Only elastic collisions are therefore permitted in the limit $\alpha\to0$. As α increases to unity, the classically forbidden zones diminish and the collision becomes more and more effective in its ability to induce larger angular momentum changes.

Figure 7 presents corresponding maps to Fig. 6. The same characteristic regions are now displayed in the plane of final reduced angular momentum ℓ'/n and the Stark parameter α for four values of the initial reduced angular momentum $\ell/n=0.071$, 0.36, 0.64, and 0.93. Again, the classically forbidden regions (gray zones) correspond to the condition $\mathcal{B}<0$ in the left upper and lower corners. The elastic $\ell'=\ell$ transitions are always possible, even when $\alpha\to0$. Again, along the solid $(\mathcal{A}=0)$ and dotted $(\mathcal{B}=0)$ lines, the transition probabilities have cusp and step singularities. When α increases, the span of the possible final angular momentum, for given angular momentum, increases. Large angular momentum transfer is only possible for collisions with large Stark parameter $\alpha\to1$. Both Figs. 6 and 7 are key to the interpretation of the variation of the probabilities $P_{\ell'\ell}(\alpha)$ with both ℓ' and α, respectively.

The result (35) obtained from the $\ell\to0$ limit of the general result (34) can be also proven directly. Because $\mathbf{L}=0$, the classical orbits are characterized only by the Runge-Lenz vector $\mathbf{A}$. In this case, the volume occupied by the initial state is

$$\mathcal{V}_{n0}=\int\delta(|\mathbf{A}|-n\hbar)\,d\mathbf{A}=4\pi n^2\hbar^2.$$

The volume of the accessible final states ℓ' is

$$\mathcal{V}_{n0\ell'}=\int\delta(|\mathbf{A}|-n\hbar)\,\delta\left(\frac{1}{2}\left|(\tilde{U}_M-\tilde{U}_N)\mathbf{A}\right|-\ell'\hbar\right)d\mathbf{A},$$

where the orthogonal matrices $\tilde{U}_{M,N}$ depend only on the Stark parameter α and are defined by Eq. (25). In a spherical coordinate system where the z axis is along the principal direction $\boldsymbol{\nu}$ of the rotation matrix $\tilde{U}_N^T\tilde{U}_M$ (as discussed earlier in this section), the magnitude is

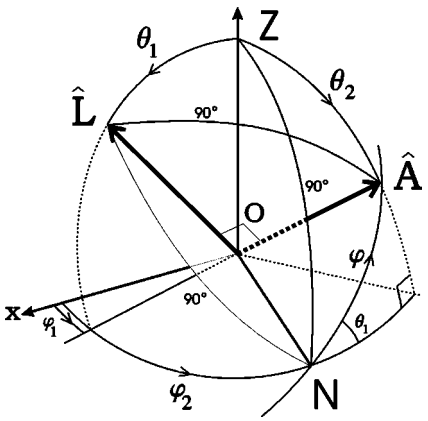

FIG. 8. The geometry of the initial state described by the directions of the angular momentum $\hat{L}$ and Runge-Lenz $\hat{A}$ vectors.

$$\frac{1}{2}|\tilde{U}_M\mathbf{A}-\tilde{U}_N\mathbf{A}|=n\hbar\sin(\chi/2)\sin\theta,$$

where θ is the angle between $\tilde{U}_M\mathbf{A}$ (or $\tilde{U}_N\mathbf{A}$) and the direction $\boldsymbol{\nu}$. The transition probability is then

$$P_{\ell'0}=\tfrac{1}{2}\int_0^\pi\delta(n\hbar\sin(\chi/2)\sin\theta-\ell'\hbar)\sin\theta\,d\theta$$

$$=\frac{\ell'/(\hbar n^2)}{\sin(\chi/2)\sqrt{\sin^2(\chi/2)-(\ell'/n)^2}},$$

in agreement with the $\ell\to0$ limit (35) to the general classical $\ell\to\ell'$ transition probability (34).

V. CLASSICAL DYNAMICS SIMULATION

The present classical Monte Carlo simulations are different from the standard classical trajectory Monte Carlo simulations in that the initial state is not specified by the position and the velocity of the orbiting electron. Instead, the simulation begins with a random distribution of the initial states in the $\{\mathbf{L}\}\otimes\{\mathbf{A}\}$ space, propagates each state according to the rule (28), and then performs the statistical analysis of the final distribution of states to provide, in the limit of an infinite number of trials, the probability $P_{\ell'\ell}$ for a given transition. This section describes the correct way to generate the initial distribution of states.

The angular momentum $\mathbf{L}$ and the Runge-Lenz $\mathbf{A}$ vectors are sufficient to completely specify all characteristics of the atom's orbit, provided they are orthogonal, as for the case of pure Coulomb attraction. Only five components are therefore independent and two of them, the magnitudes L and $A=\sqrt{n^2-L^2}$, characterize the shape and size of the orbit. There are then three angles that specify the orientation of the orbit in space, for a given assignment of the energy and angular momentum. The direction of the angular momentum vector $\hat{L}$ is arbitrary. Two random numbers, the projection

$L_z=\cos\theta_1$ and its azimuthal angle φ_1, generate a uniform distribution of $\hat{L}$ on the unit sphere. The direction of the Runge-Lenz vector $\hat{A}$ is uniformly distributed in the plane perpendicular to $\hat{L}$, and the angle φ between $\hat{A}$ and a given fixed direction $\hat{N}$ in this plane is the third random number required to simulate an initial state. In summary, three random numbers are required: (i) $L_z=\cos\theta_1$ uniformly distributed within the $[-1,1]$ interval, (ii) φ_1 uniformly distributed within the $[0,2\pi]$ interval, and (iii) φ uniformly distributed within the $[0,2\pi]$ interval. The initial **L** and **A** vectors are then

$$\mathbf{L}=\hbar\ell\begin{pmatrix}\sin\theta_1\cos\varphi_1\\ \sin\theta_1\sin\varphi_1\\ \cos\theta_1\end{pmatrix},\quad \mathbf{A}=\hbar\sqrt{n^2-\ell^2}\begin{pmatrix}\sin\theta_2\cos\varphi_2\\ \sin\theta_2\sin\varphi_2\\ \cos\theta_2\end{pmatrix}.$$

The spherical polar angles θ_2 and φ_2 of **A**, as illustrated in Fig. 8, must now be expressed in terms of the above random variables θ_1, φ_1, and φ. Basic trigonometry [32] applied to the spherical triangles $Z\hat{N}\hat{A}$ and $\hat{L}Z\hat{A}$ yields

$$\cos\theta_2=\sin\varphi\sin\theta_1$$

and

$$0=\cos\theta_1\cos\theta_2+\sin\theta_1\sin\theta_2\cos(\varphi_2-\varphi_1),$$

respectively. On solving these two equations for θ_2 and φ_2, the arbitrary Runge-Lenz vector

$$\mathbf{A}(\theta_1,\varphi_1,\varphi)=\hbar\sqrt{n^2-\ell^2}\begin{pmatrix}-\cos\theta_1\cos\varphi_1\sin\varphi-\sin\varphi_1\cos\varphi\\ -\cos\theta_1\sin\varphi_1\sin\varphi+\cos\varphi_1\cos\varphi\\ \sin\theta_1\sin\varphi\end{pmatrix}$$

is then expressed in term of the random variables. It automatically obeys the constraint requirements $\mathbf{A}\cdot\mathbf{L}=0$, $A^2+L^2=n^2$, and $\hat{A}\cdot\hat{N}=\cos\varphi$.

VI. NUMERICAL EXAMPLES

In this section, numerical examples for calculation of the transition probability between states with given angular momentum ($n\ell\to n\ell'$) are presented. There are three main methods used in this paper. The classical Monte Carlo simulation, as described in the preceding section, requires the running of a large number of trials to sample the three dimensional space of arbitrary parameters. The explicit classical mechanics expression (34) is used directly.

The quantal calculation is based on Eqs. (13) and (12). A matrix representation for the operator $L_1-\alpha A_3$ [where Pauli's replacement (5) was adopted] is required. Instead of the spherical basis $|\ell m\rangle$, which is difficult to use in this case, we define a new linear basis obtained by mapping the (l,m) quantum numbers to a unique index $k=\ell^2+\ell+m+1$, in such a way, for example, that $(0,0)\to1$, $(1,-1)\to2$, $(1,0)\to3$, $(1,1)\to4$, $(2,-2)\to5$, and so on. The inverse mapping is given by $\ell=\text{floor}(\sqrt{k-1})$ and $m=k-\ell^2-\ell-1$. The index k counts the degeneracy of the energy shell, and runs from 1 to n^2. The matrix element

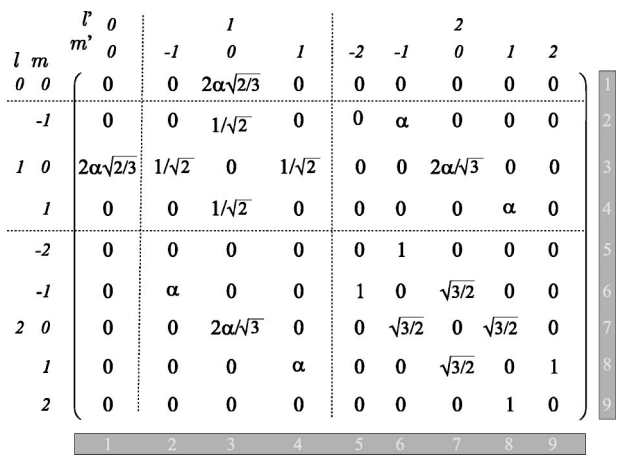

FIG. 9. Matrix representation of $L_1-\alpha A_3$ for $n=3$.

$$(L_1)^{\ell' m'}_{\ell m}=\tfrac{1}{2}\sqrt{(\ell+m)(\ell-m+1)}\,\delta_{\ell'\ell}\delta_{m',m-1}+\tfrac{1}{2}\sqrt{(\ell-m)(\ell+m+1)}\,\delta_{\ell'\ell}\delta_{m',m+1}$$

of L_1 is nonzero only for $\Delta\ell=0$ and $\Delta m=\pm1$, which reflects the fact that the cylindrical symmetry of the Rydberg atom is broken by the precession of **L** about the field of the projectile. These *m-changing* transitions are, however, conditioned by the full structure of solution (12), which shows that such transitions are only in evidence for nonzero α. The matrix element

$$(A_3)^{\ell' m'}_{\ell m}=-\sqrt{\frac{(\ell^2-m^2)(n^2-\ell^2)}{(2\ell+1)(2\ell-1)}}\,\delta_{\ell'\ell-1}\delta_{m',m}-\sqrt{\frac{[(\ell+1)^2-m^2][n^2-(\ell+1)^2]}{(2\ell+3)(2\ell+1)}}\,\delta_{\ell'\ell+1}\delta_{m',m}$$

of the component $A_3=-(2/3n)z$ along the fixed Z axis of quantization is nonzero for $\Delta\ell=\pm1$ and $\Delta m=0$ transitions. These dipole transitions only contribute for nonzero α. The matrix $L_1-\alpha A_3$ has then a band diagonal structure, as illustrated in Fig. 9 for the special case of $n=3$. Explicit analytical formulas for $P^{(n)}_{\ell'\ell}(\alpha,\Delta\Phi)$ can be directly obtained [33] for small $n=2,3$.

The transition amplitude for transition $k\to k'$ is the kk' matrix element of the exponential of the matrix $-i\Delta\Phi(L_1-\alpha A_3)$, sandwiched between the rotations implied by Eq. (12). When $\alpha\approx0$, the dipole forbidden transitions are not possible, because the transition matrix $\approx\exp i\pi L_1/\hbar$ still maintains a band diagonal structure. As α increases, more and more off-diagonal elements become populated, leading to dipole forbidden transitions. Efficient algorithms, using Padé approximations, are available [27] for matrix exponentiation. The full array of transition probabilities is then obtained all at once.

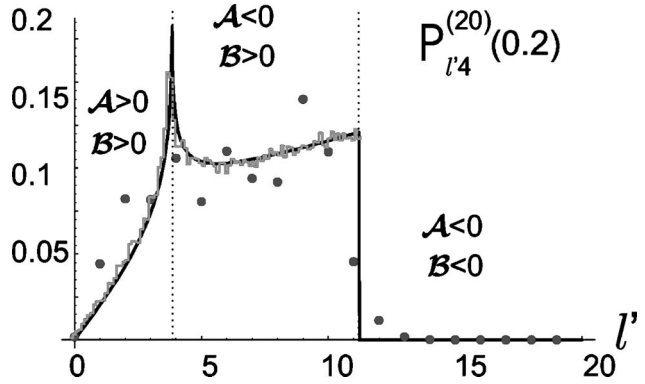

FIG. 10. The Monte Carlo simulation (steplike lines), the classical (solid line), and quantal (dots) transition probabilities $P_{\ell'\ell}(\alpha)$ for given $\alpha=0.2$ and initial $\ell=4$ within the $n=20$ shell.

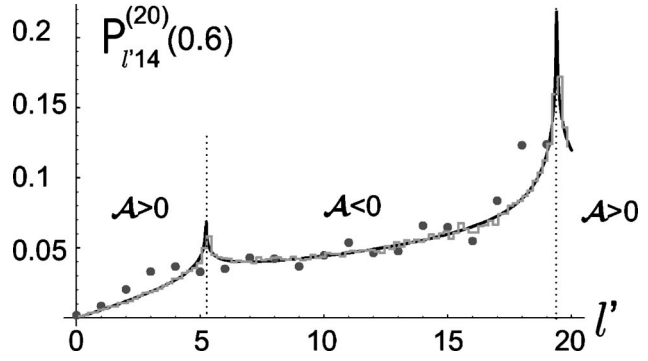

FIG. 12. The Monte Carlo simulation (steplike lines), the classical (solid line), and quantal (dots) transition probabilities $P_{\ell'\ell}(\alpha)$ for given $\alpha=0.6$ and initial $\ell=14$ within the $n=20$ shell. $\mathcal{B}>0$ for all ℓ'.

The examples, provided by Figs. 10–13, demonstrate that the Monte Carlo simulation yields results identical to the classical dynamics expression (34). The transition probabilities for given Stark parameters ($\alpha=0.2$ and 0.6) and initial angular momentum ($\ell=4$, 12, 14, and 18, respectively) are represented as a function of the final angular momentum ℓ'. This also provides the distribution over the final angular momentum states, which result from collisions, at given α, from an initial population of states with the same initial angular momentum ℓ. In this example, $n=20$. The present corresponding quantal results are also represented in the same graphs by dots. Vertical dotted lines indicate the positions of the singularities, corresponding to the $\mathcal{A}=0$ and $\mathcal{B}=0$ lines in Fig. 6. The $\mathcal{A}=0$ and $\mathcal{B}=0$ singularities produce cusp and step variations in $P_{\ell'\ell}$ as ℓ' increases through the singularity (Fig. 6). Four distinct and characteristic classes of variation of $P_{\ell'\ell}$ with ℓ' then emerge. These are displayed in Figs. 10–13, where the predicted (cusp,step), (step,step), (cusp,cusp), and (step,cusp) classical variations are exhibited. These results are fully representative and can be analyzed by vertical cuts through Fig. 6 appropriate to a given ℓ. The ℓ and α parameters in Figs. 10–13 correspond to the values $\ell/n=0.2$ and 0.6 and to $\ell/n=0.7$ and 0.9 in the first and third plots of Fig. 6, respectively. The steps indicate a classical threshold ℓ'_- or a classical cutoff ℓ'_+ for transitions to a final value of ℓ'. The cusp-step variation of Fig. 10 indicates that transitions to $\ell'\leqslant\ell'_+$ are classically allowed and the step-step variation of Fig. 11 indicates that classically accessible ℓ' are within the range $\ell'_-\leqslant\ell'\leqslant\ell'_+$. The cusp-cusp variation of Fig. 12 is associated with the fact that transitions to all ℓ' are classically accessible (cf. Fig. 6, plot 3), while the step-cusp variation of Fig. 13 signifies that only transitions to $\ell'\geqslant\ell'_-$ are classically possible. For a given initial angular momentum ℓ and Stark parameter α, the position of the cusp singularities, given by the solutions of the equation $\mathcal{A}=0$, is

$$\left(\frac{\ell'_\pm}{n}\right)=\left|\left(1-\frac{\ell^2}{n^2}\right)^{1/2}\sin\frac{\chi}{2}\pm\left(\frac{\ell}{n}\right)\cos\frac{\chi}{2}\right|. \tag{36}$$

Expressions (36) are also solutions of the equation $\mathcal{B}=0$ for the step singularities. The threshold value ℓ'_- is a cusp (solution of $\mathcal{A}=0$) provided $\ell<n\sin\chi/2$ and is a step (solution of $\mathcal{B}=0$) provided $\ell>n\sin\chi/2$. Similarly, the cutoff ℓ'_+ is

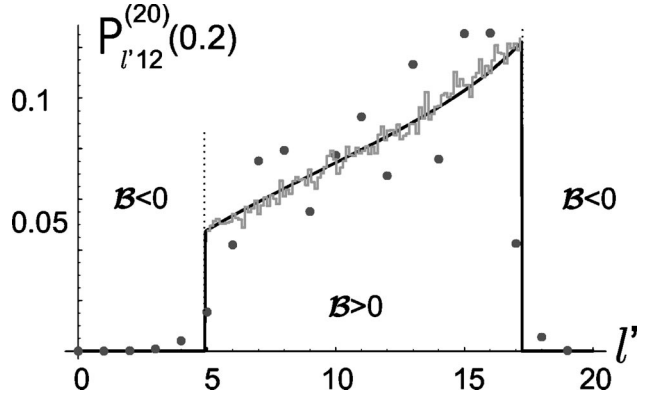

FIG. 11. The Monte Carlo simulation (steplike lines), the classical (solid line), and quantal (dots) transition probabilities $P_{\ell'\ell}(\alpha)$ for given $\alpha=0.2$ and initial $\ell=12$ within the $n=20$ shell. $\mathcal{A}<0$ for all ℓ'.

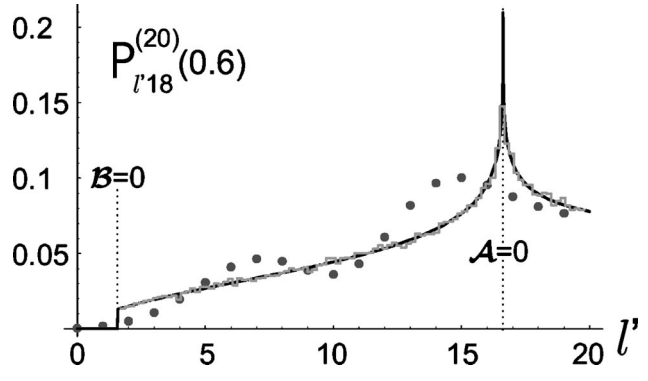

FIG. 13. The Monte Carlo simulation (steplike lines), the classical (solid line), and quantal (dots) transition probabilities $P_{\ell'\ell}(\alpha)$ for given $\alpha=0.6$ and initial $\ell=18$ within the $n=20$ shell. Across the first dotted line $\mathcal{B}$ changes sign and $\mathcal{A}$ is negative on both sides of this line. $\mathcal{A}$ changes sign across the second line while $\mathcal{B}$ remains positive.

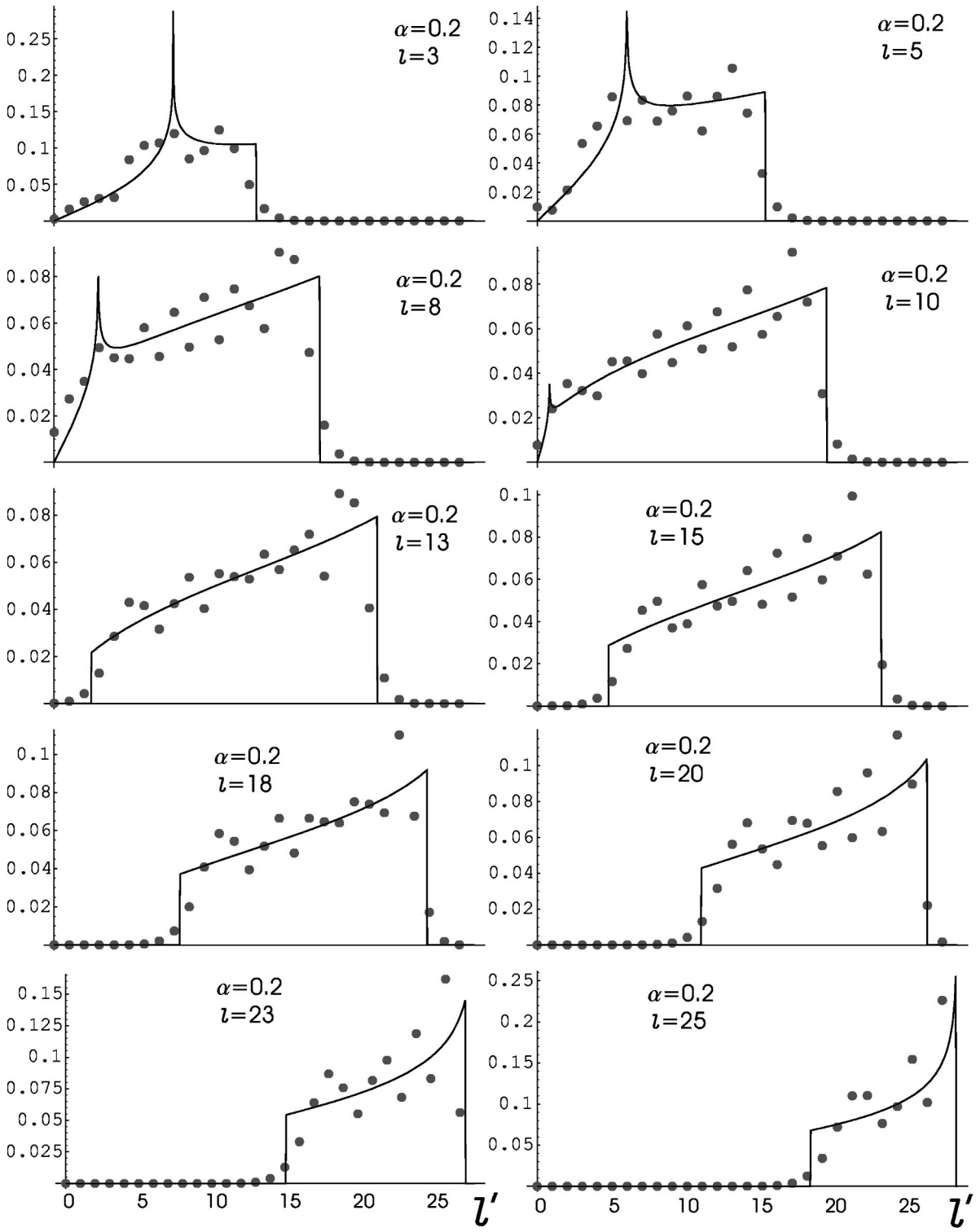

FIG. 14. The classical and quantal Stark mixing transition probabilities $P_{\ell'\ell}(\alpha)$ within the $n=28$ energy shell, for $\alpha=0.2$, as a function of the final angular momentum ℓ' and for various initial angular momenta ℓ.

a cusp if $\ell > n\cos\chi/2$ or a step if $\ell < n\cos\chi/2$. The separation between the singularities is

$$\left(\frac{\ell'_+}{n}\right)-\left(\frac{\ell'_-}{n}\right)=2\left(1-\frac{\ell^2}{n^2}\right)^{1/2}\sin\frac{\chi}{2}$$

when $\ell/n \geqslant \sin\chi/2$, and is

$$\left(\frac{\ell'_+}{n}\right)-\left(\frac{\ell'_-}{n}\right)=2\left(\frac{\ell}{n}\right)\cos\frac{\chi}{2}$$

when $\ell/n \leqslant \sin\chi/2$. The maximum separation of $\sin\chi$ is attained at $\ell^*/n=\sin\chi/2$. This occurs in Fig. 6 where the $\mathcal{A}=0$ and $\mathcal{B}=0$ curves both intersect the ℓ/n axis at ℓ^*/n. The transitions $\ell \to \ell'$ have significant quantal probabilities

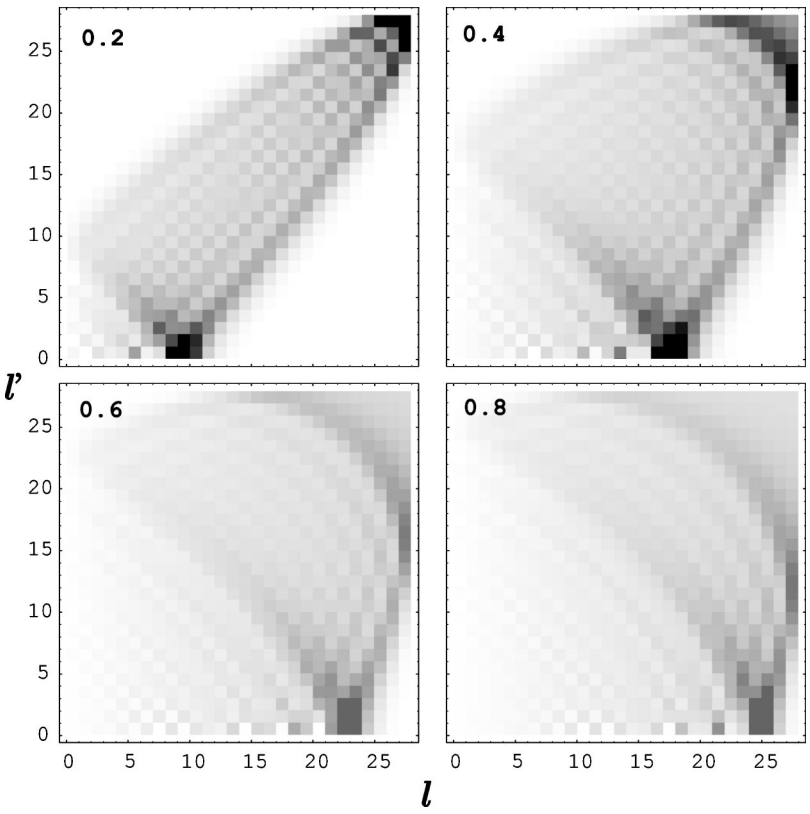

FIG. 15. Density plots of the transition probabilities, calculated within the quantal treatment, for four values of $\alpha=0.2$, 0.4, 0.6, and 0.8 in the (ℓ,ℓ') plane. The probability increases as the gray becomes darker.

only when ℓ' is in the classical accessible region and exhibit the characteristic exponential decreasing behavior in the classical inaccessible regions.

The second set of examples compares between the classical and quantal transition probabilities within the $n=28$ energy shell. A set of graphs, for various ℓ and fixed Stark parameter $\alpha=0.2$, is presented in Fig. 14. The transition probability is plotted versus the final angular momentum. The cusp-step, step-step, and step-cusp variations are all apparent, together with the superimposed quantal oscillatory behavior within the classical accessible region. The oscillations possibly originate from the fact that there are two points **N** of intersection of the two arcs (drawn on the sphere of Fig. 5) with centers **M** and **M**″ with separation $\Gamma(\alpha)$ and radii $u_1(\ell)$ and $u_2(\ell')$. Each point of intersection provides equal classical contributions to $P_{\ell'\ell}(\alpha)$ while the different phases associated with each point produce the quantal (semiclassical) interference oscillations, exhibited in both the ℓ' variations of $P_{\ell'\ell}(\alpha)$ with ℓ and α fixed, as in Fig. 14, and the α variation of $P_{\ell'\ell}(\alpha)$ in Fig. 16 for ℓ and ℓ' fixed. Figure 14 also illustrates that the separation $(\ell'_+-\ell'_-)/n$ between the various discontinuities increases to $\sin\chi$ at $\ell/n=\sin\chi/2$ and then decreases as ℓ is increased from 0 to $n-1$, in accord with Eq. (36). In general, Fig. 14 shows that the classical picture is complementary to the quantal in that it has the ability to explain the general overall behavior of the quantal results and to provide the general framework on which the quantal results rest. It has also provided the various regions (between cusps, steps, etc.) that remain obscured within the quantal treatment.

The set of plots in Fig. 15 is the quantal correspondent of the similar classical set of plots presented in Fig. 6. Density maps in the (ℓ,ℓ') plane are shown for the same four values of Stark parameter α. The first map for $\alpha=0.2$ corresponds to the results of Fig. 14, where cuts along various values of ℓ/n are made. The quantal transition probability increases as the gray areas becomes darker. The same zones outlined in Fig. 6 can be recognized and the boundaries between them are in exact correspondence with the classical equations $\mathcal{A}=0$ and $\mathcal{B}=0$, as discussed at the end of Sec. V. The quantal transition probabilities are practically zero over the classical forbidden regions, occupying the upper left and lower right corners of Fig. 6. The quantal probabilities are maximum on the ridge given by the equation $\mathcal{A}=0$, where the classical dynamics results in singularities.

When α is very small, decreasing toward zero, only elastic transitions are allowed so that only the principal diagonal is exhibited, as in Figs. 6 and 15. The quantal calculation yields unity for the probability of elastic $\ell=\ell'$ transitions in the $\alpha\to0$ limit and the classical result diverges as $1/\alpha$ in the same limit. All other transitions have zero probability. This feature is responsible for the well known [4] divergence of the cross section (6) for elastic transitions.

Figure 16 displays the probability for transitions originating from the initial level $\ell=5$ to various final levels, as a function of the Stark parameter α. Again, the agreement is expectedly very good. For small α, there is always a classical inaccessible region ($\mathcal{B}<0$) for quasielastic $\ell'\neq\ell$, except for the fully elastic transitions $\ell'=\ell$. A threshold step at $\alpha=\alpha_T$ is therefore displayed for the probability of transitions with $\ell'=\ell$. This property is fully explained with the

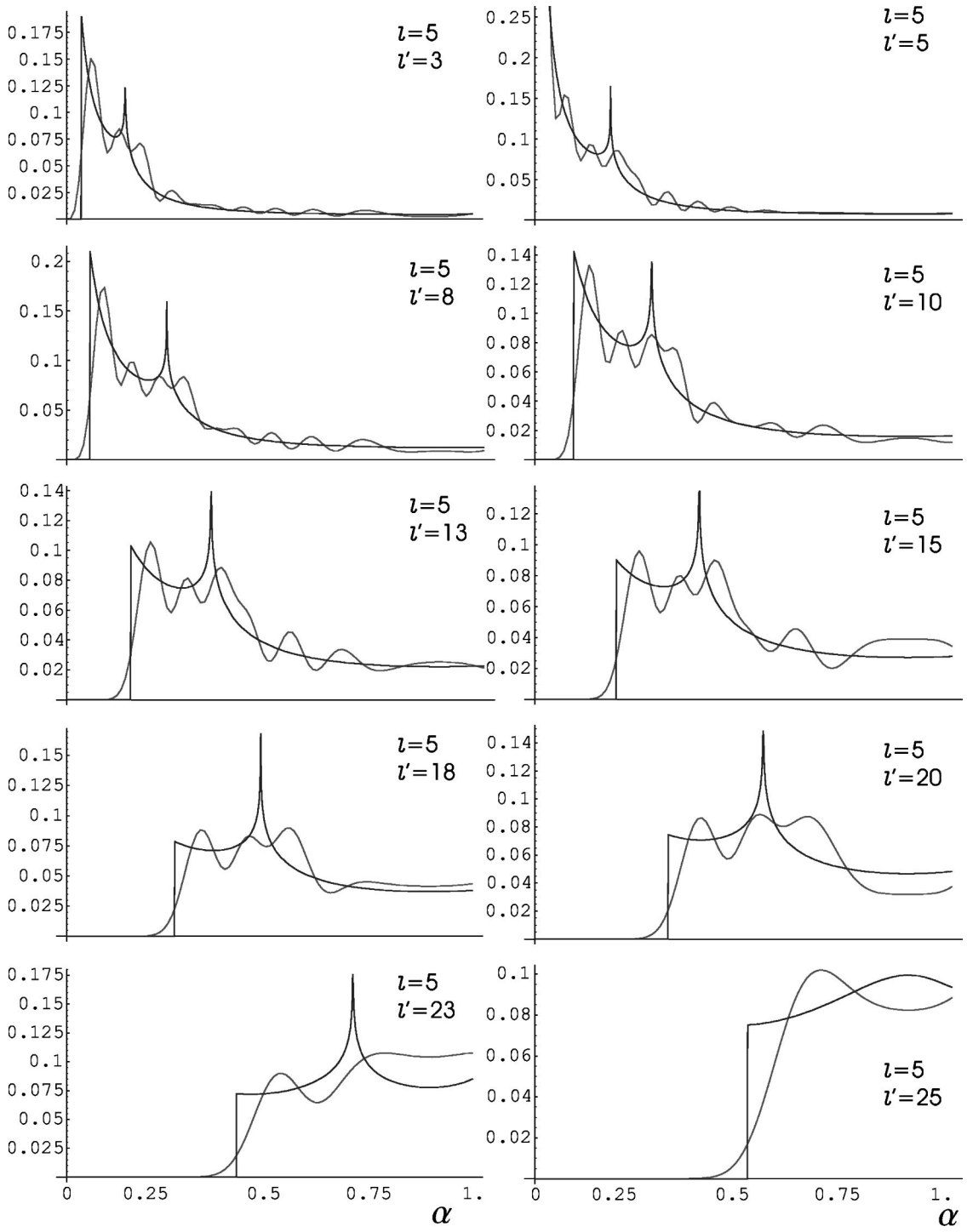

FIG. 16. The classical and quantal Stark mixing transition probabilities $P_{\ell'\ell}(\alpha)$ within the $n=28$ energy shell, for $\ell=5$, as a function of the Stark parameter α and for various final angular momenta ℓ'.

aid of the plots in Fig. 7 of ℓ'/n versus α for various values of ℓ/n. As ℓ' is increased, α_T determined by the intersection of ℓ'/n with the $\mathcal{B}=0$ curve increases and a step ($\mathcal{B}=0$) to cusp ($\mathcal{A}=0$) variation with α is obtained, as exhibited in Fig. 16. For higher ℓ'/n values, intersection with the $\mathcal{A}=0$ curve (and therefore the cusp) disappears. Figure 16 (for the specific $n=28$ case considered, or in general Fig. 7) also shows that low $\ell\rightarrow$ high ℓ' and high $\ell\rightarrow$ low ℓ' transitions are precluded ($\mathcal{B}<0$) except at high values of $\alpha\rightarrow 1$.

Figure 17 shows that the quantal probabilities are high in the classical accessible regions ($\mathcal{B}>0$) of Fig. 7 and are more significant in the $\mathcal{A}<0$ region than in the $\mathcal{A}>0$ region. Variation of the transition probability along the horizontal line for $\ell'=$const provides plots as exhibited in Fig. 16. Figure 17 is the quantal correspondence of Fig. 7.

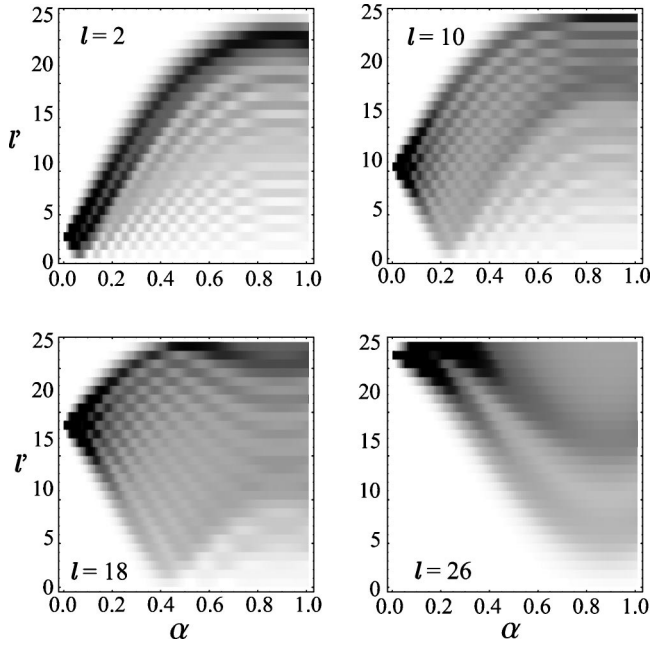

FIG. 17. Density plots of the transition probabilities, calculated within the quantal treatment, for four values of the initial angular momentum $\ell = 2$, 10, 18, and 26, in the (α, ℓ') plane. The probability increases as the gray becomes darker.

Figure 18 exhibits variation of the integral factor

$$I^{(n)}_{\ell'\ell} = \int_{\alpha_{\min}}^{1} P^{(n)}_{\ell'\ell} \frac{d\alpha}{\alpha^3} = \frac{\sigma_{\ell'\ell}}{\pi a_n^2} 2\left(\frac{v}{3Z_1 v_n}\right)^2,$$

which appears in the cross section (6) as a function of the final angular momentum ℓ' for various initial angular momenta ℓ. It is assumed here that $\Delta\Phi = -\pi$. This integral does not depend on the projectile properties (velocity, impact parameter, or charge) but depends only on the initial and final state of the target. Due to the $1/\alpha^3$ singularity, the cross sections for elastic ($\ell = \ell'$) and near elastic transitions are very much enhanced. Various cutoff ($\alpha_{\min}$) procedures can be introduced from physical considerations specific to the actual problem discussed. For the results presented in Fig. 18, an arbitrary cutoff $\alpha_{\min} = 0.01$ was introduced for both the classical and quantal calculations. With the exception of elastic transitions, where special care must be exercised since the present model fails, the agreement between quantal and classical model is much better than one would expect from the traditional correspondence principles such as Ehrenfest's theorem and Bohr's correspondence. The exceptionally rich symmetry group SO(4), characteristic for one-electron atoms in both the quantal and classical treatments, explains the quality of the agreement obtained.

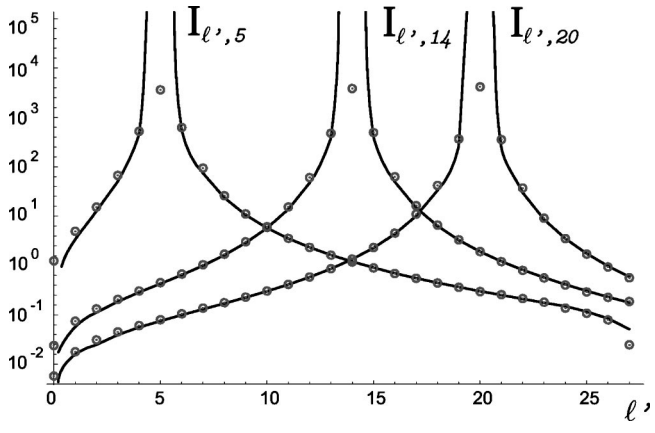

FIG. 18. Classical and quantal comparison of the integral $I_{\ell'\ell}$ defining the Stark mixing cross section (6) within the $n = 28$ energy shell, for various initial angular momenta ℓ as a function of the final angular momentum ℓ'.

VII. CONCLUSIONS

In conclusion, we have presented a case study of the long-standing problem of the $n\ell \to n\ell'$ transition array in atomic hydrogen produced by distant collisions with slow heavy charged particles. Complete formulations from the quantal, classical, and Monte Carlo simulation viewpoints have been developed. The SO(4) dynamical symmetry of H(n) has been exploited to provide exact classical and quantal solutions (28) and (12), under the adiabatic, dipole and classical path assumptions. A classical expression (31) for the transition probability $P^{(n)}_{\ell'\ell}$ is presented in a language that exploits the dynamical symmetry and is used to obtain exact analytical results (34). A new exact (fixed-frame) representation Eq. (12) of the quantal solution has also been presented and directly applied to provide exact quantal probabilities for the full array of transitions. This solution is feasible for efficient numerical calculation of probabilities for transitions involving even large n and all ℓ and ℓ', in contrast to the previous quantal (rotating-frame) version [15,16], which was applied only to the $\ell = 0 \to \ell'$ transitions. Exact analytical expressions for $P^{(n)}_{\ell'\ell}$ can also be obtained [33] for low n.

The exact quantal results for $P^{(n)}_{\ell'\ell}$ oscillate about the classical background. By revealing essential characteristics that remain obscured within the quantal treatment, the classical results complement the quantal results. Further development would include a semiclassical analysis capable of reproducing the oscillatory structure in the quantal $P^{(n)}_{\ell'\ell}$ without sacrificing the physical transparency of the classical model.

Although the numerical results presented here are associated with a straight line projectile path (i.e., $\Delta\Phi = -\pi$), the theory is suitable for all polar deflection angles $\Delta\Phi$ swept out during the collision by the classical trajectory. Specific problems (nonhydrogenic atoms, stray fields, the Debye radius in plasmas, etc.) may impose further restrictions on the range of impact parameter b, which results in restrictions on α. The basic theory presented can still be applied to these cases with minor adjustments. The classical trajectory appropriate to a rotating dipole can be determined to account for the influence of the target on the projectile's motion.

In summary, both classical and quantal solutions of Stark mixing have been presented in a compact form reflecting the mathematical beauty of the problem as well as their pragmatic value. It is probably one of the last remaining problems in collision physics capable of an exact solution.

Note added in proof. A general concise analytical expression for the quantal probabilities $P^{(n)}_{\ell'\ell}$ for all n has since been obtained [34] in a form (a) which is easy to use for numerical evaluation, even at very high $n\sim 100$, (b) which yields compact analytical results for $n=2-5$ and (c) which naturally provides the classical limit (34) obtained here.

ACKNOWLEDGMENTS

This work has been supported by AFOSR Grant No. 49620-99-1-0277 and NSF Grant No. 98-02622.

APPENDIX A: PAULI'S REPLACEMENT

Pauli's replacement [23] for the classical one-electron atom follows from the straightforward calculation of the averaged projection of the position vector on the Runge-Lenz vector,

$$\langle \mathbf{r}\cdot\hat{\mathbf{A}}\rangle = \frac{3}{2}\epsilon\frac{e^2}{2E} = -\frac{3}{2}A\frac{1}{\sqrt{-2m_eE}},$$

where ϵ is the eccentricity of the orbit corresponding with the energy E. Because the perpendicular component of $\mathbf{r}$ on $\mathbf{A}$ averages to zero, the following rule is valid, *on averaging* over an orbital period:

$$\mathbf{r}\approx -\frac{3}{2}\frac{\mathbf{A}}{p_n}$$

provided $\mathbf{A}$ does not change significantly in this time. Here $p_n=\sqrt{\langle p^2\rangle}=\sqrt{-2m_eE}$ is the characteristic orbital momentum.

The classical Runge-Lenz vector has the symmetrized (Pauli-Lenz) quantal form

$$\mathbf{A}=\left[\frac{1}{2}(\mathbf{p}\times\mathbf{L}-\mathbf{L}\times\mathbf{p})-m_ee^2\hat{r}\right]\Big/\ p_n$$

alternative to the form given by Eq. (1). The operator $\mathbf{A}$ has the following properties:

$$[A_j,H]=0 \quad \text{(a conserved quantity)},$$

$$[L_j,A_k]=i\hbar\epsilon_{jkn}A_n \quad \text{(also a vector)},$$

$$[A_j,A_k]=i\hbar\epsilon_{jkn}L_n \quad \text{(its components do not commute)},$$

$$\mathbf{A}\cdot\mathbf{L}=\mathbf{L}\cdot\mathbf{A}=0 \quad \text{(vector } \mathbf{A} \text{ is orthogonal on } \mathbf{L}),$$

$$A^2+L^2=(n^2-1)\hbar^2 \quad \text{(constant for intrashell transitions)}.$$

These commutation relations define the SO(4) dynamic symmetry group for the restricted motion of the orbital electron to the energy shell. The Hamiltonian H is an invariant and can be used to label matrix representations for this group. The correct energy levels for the hydrogen atoms result from the symmetry without solving any differential equation. The SO(4) operators can be disentangled by introducing $\mathbf{M}=(\mathbf{L}+\mathbf{A})/2$ and $\mathbf{M}=(\mathbf{L}-\mathbf{A})/2$. Each $\mathbf{M}$ and $\mathbf{N}$ operators generate separately a so(3) subalgebra, such that $\mathrm{SO}(4)\equiv\mathrm{SO}(3)\oplus\mathrm{SO}(3)$.

Following [26], it is useful to prove the following.

Result. The matrix elements of the operators $\mathbf{\Omega}$ defined by

$$\mathbf{\Omega}=\mathbf{r}+\frac{3}{2}\frac{\mathbf{A}}{p_n}$$

are zero between any states with the same energy, i.e., $\mathbf{\Omega}\equiv 0$ within the energy shell.

Proof. The commutator between the Pauli-Lenz vector and the position vector can be written as

$$[A_j,r_k]=-\frac{3}{2p_n}i\hbar\epsilon_{jkn}L_n+\frac{1}{2p_n}[m_eH,r_jr_k-r^2\delta_{jk}]. \tag{A1}$$

Because the commutator $[H,X]$ is zero for any Hermitian operator X, when restricted to the energy shell (*the hypervirial theorem* [35]), commutator (A1) is simply

$$[A_j,r_k]=-\frac{3}{2p_n}i\hbar\epsilon_{jkn}L_n$$

in the Hilbert subspace of degenerate states with the same energy. Thus, the vector $\mathbf{\Omega}$ commutes with the Pauli-Lenz vector and has the commutators

$$[M_j,\Omega_k]=[N_j,\Omega_k]=\frac{1}{2}i\hbar\epsilon_{jkn}\Omega_n$$

with the vectors $\mathbf{M}$ and $\mathbf{N}$ obtained by decomposition (2). With the aid of the basic Jacobi identity for commutators,

$$[A,[B,C]]+[B,[C,A]]+[C,[A,B]]=0,$$

it follows directly that $\mathbf{\Omega}=\mathbf{0}$. For example, $\Omega_2=0$ if $A=M_3$, $B=N_2$, and $C=\Omega_3$.

This result provides a concise proof that Pauli's replacement (5) is valid whenever the dynamics is constrained to the constant energy manifold (cf., [18] for a lengthier proof).

APPENDIX B: AREA ELEMENT FOR SPHERICAL BIFOCAL COORDINATES

The spherical bifocal coordinates are given by the angles u_1 and u_2 between a point (P) and two fixed foci (A_1 and A_2) on the unit sphere. Of course, these coordinates are unique only on the half sphere.

Theorem. The area element in spherical bifocal coordinates is

$$dS=\frac{du_1\,du_2}{\sin\Delta},$$

where Δ is the angle between the arcs joining a given point on the sphere with the two foci:

$$\Delta = \angle \mathrm{A}_1\mathrm{PA}_2 .$$

Proof. Here are two proofs of the theorem. One is short and intuitive. The other one is longer but a bit more rigorous.

Short Proof. The length of the arc described by the point **P** on the sphere for an infinitesimal change $u_2 \rightarrow u_2 + du_2$, when u_1 is kept fixed, is ds_1. Basic spherical triangle geometry provides

$$ds_1 = \frac{du_2}{\sin\Delta}$$

and a similar relation

$$ds_2 = \frac{du_1}{\sin\Delta}$$

for the infinitesimal arc ds_2. The elementary surface area is given by the cross product of the two arcs $d\mathbf{s}_1 \times d\mathbf{s}_1$. Since the angle between these arcs is, in the first order of approximations, again Δ, then

$$dS = \frac{du_1\, du_2}{\sin\Delta},$$

as advertised.

Direct Proof. A direct proof calculates by brute force the area element using

$$dS = \left| \frac{\partial \vec{P}}{\partial u_1} \times \frac{\partial \vec{P}}{\partial u_2} \right| du_1 du_2 . \tag{B1}$$

The length of the calculation depends, of course, on the particular coordinate frames of choice. For example, one can choose A_1 and A_2 in the equatorial xOy plane, with A_1 on the Ox axis. Let D be a point on the arc A_1A_2 such that the arc PD is perpendicular to A_1A_2 (like a meridian passing through P). The coordinates of the point P are then

$$P := (\cos\theta\cos\phi,\ \cos\theta\sin\phi,\ \sin\theta),$$

where $\theta = \angle PD$ and $\phi = \angle A_1D$. Applying again spherical trigonometry to the spherical triangles A_1PD and A_2PD, then

$$P := (\cos u_1, \sqrt{\cos^2 \angle \mathrm{PD} - \cos^2 u_1},\ \sin\angle \mathrm{PD}),$$

where

$$\sin\angle \mathrm{PD} = \sin u_1 \sin u_2 \sin\Delta / \sin\Gamma ,$$

where, by definition, $u_{1,2} = \angle \mathrm{A}_{1,2}\mathrm{P}$, $\Delta = \angle \mathrm{A}_1\mathrm{PA}_2$, and $\Gamma = \angle \mathrm{A}_1\mathrm{A}_2$. The goal is to express all coordinates of P in terms of u_1 and u_2 and to do the corresponding derivatives in Eq. (B1). Spherical trignometry yields

$$\begin{aligned} S^2 &= \sin^2 u_1 \sin^2 u_2 \sin^2\Delta \\ &= [\cos(u_1 - u_2) - \cos\Gamma][\cos\Gamma - \cos(u_1 + u_2)]. \end{aligned}$$

On defining

$$S_{\pm} = \sin\frac{1}{2}[\Gamma \pm (u_1 + u_2)],$$

$$\tilde{S}_{\pm =} \sin\frac{1}{2}[\Gamma \pm (u_1 - u_2)],$$

the angle Δ is then determined from

$$\sin\Delta = \frac{S}{\sin u_1 \sin u_2} = 2\,\frac{\sqrt{S_+ S_- \tilde{S}_+ \tilde{S}_-}}{\sin u_1 \sin u_2}$$

and the coordinates of P are now

$$P := \left[\cos u_1,\ \frac{S_+\tilde{S}_+ - S_-\tilde{S}_-}{\sin\Gamma},\ 2\,\frac{\sqrt{S_+ S_- \tilde{S}_+ \tilde{S}_-}}{\sin\Gamma} \right].$$

Then Eq. (B1) finally reduces to

$$dS = \left[\frac{\sin u_1 \sin u_2}{S} \right] du_1\, du_2 = \frac{du_1\ du_2}{\sin\Delta},$$

which proves directly the above theorem for spherical bifocal coordinates.

[1] M. Leon and H.A. Bethe, Phys. Rev. **127**, 636 (1962).

[2] J.E. Miraglia and J. Macek, Phys. Rev. A **42**, 3971 (1990).

[3] F. Merkt and R.N. Zare, J. Phys. Chem. **101**, 3495 (1994).

[4] R.M. Pengelly and M.J. Seaton, Mon. Not. R. Astron. Soc. **127**, 165 (1964); I. Percival, *Atoms in Astrophysics* (Plenum, New York, 1983), pp. 75–102.

[5] L.I. Men'shikov and P.O. Fedichev, Zh. Éksp. Teor. Fiz. **108**, 144 (1995) [JETP **81**, 78 (1995)].

[6] M.R. Flannery and D. Vrinceanu, in *Atomic Processes in Plasmas: 11th APS Topical Conference*, edited by E. Oks and M. S. Pindzola (AIP, New York, 1998), pp. 317–333.

[7] X. Sun and K.B. MacAdam, Phys. Rev. A **47**, 3913 (1993).

[8] V.S. Lebedev and I.L. Beigman, *Physics of Highly Exited Atoms and Ions* (Springer-Verlag, Berlin, 1998); I.L. Beigman and M.I. Syrkin, Zh. Éksp. Teor. Fiz. **89**, 400 (1985) [Sov. Phys. JETP **62**, 226 (1985)].

[9] M. Born, *The Mechanics of the Atom* (Ungar, New York, 1960), p. 235.

[10] Yu.N. Demkov, B.S. Monozon, and V.N. Ostrovskiĭ, Zh. Éksp. Teor. Fiz. **57**, 1431 (1969) [Sov. Phys. JETP **30**, 775 (1970)].

[11] A.K. Kazansky and V.N. Ostrovsky, J. Phys. B **29**, L855 (1996).

[12] Yu.N. Demkov, V.N. Ostrovskiĭ, and E.A. Solov'ev, Zh. Éksp. Teor. Fiz. **66**, 125 (1974) [Sov. Phys. JETP **39**, 57 (1974)].

[13] A.K. Kazansky and V.N. Ostrovsky, Phys. Rev. A **52**, R1811 (1995).

[14] A.K. Kazansky and V.N. Ostrovsky, J. Phys. B **29**, 3651 (1996).

[15] A.K. Kazansky and V.N. Ostrovsky, Zh. Éksp. Teor. Fiz. **110**, 49 (1996) [Sov. Phys. JETP **83**, 1095 (1996)].
[16] A.K. Kazansky and V.N. Ostrovsky, Phys. Rev. Lett. **77**, 3094 (1996).
[17] P. Bellomo, D. Farrelly, and T. Uzer, J. Chem. Phys. **107**, 2499 (1995).
[18] P. Bellomo, C.R. Stroud, D. Farrelly, and T. Uzer, Phys. Rev. A **58**, 3896 (1998).
[19] C.E. Wulfman, in *Group Theory and its Applications*, edited by E.M. Loebl (Academic, New York, 1977), p. 146; B.G. Wybourne, *Classical Groups for Physicists* (Wiley, New York, 1974).
[20] H.A. Bethe and E.E. Salpeter, *Quantum Mechanics of One- and Two-electron Atoms* (Plenum, New York, 1977), p. 83.
[21] T.P. Hezel *et al.*, Am. J. Phys. **60**, 329 (1992).
[22] I.C. Percival and D. Richards, J. Phys. B **12**, 2051 (1979).
[23] W. Pauli, Z. Phys. **36**, 336 (1926).
[24] J.D. Louck, in *Atomic, Molecular, and Optical Physics Handbook*, edited by G.W.F. Drake (AIP, New York, 1996), p. 15.
[25] C.B. Tarter, J. Math. Phys. **11**, 3192 (1970).
[26] G. Flamand, J. Math. Phys. **7**, 1924 (1964).
[27] G.H. Golub and C.F.V. Loan, *Matrix Computation* (Johns Hopkins University, Baltimore, 1983), p. 384.
[28] M.R. Flannery, Phys. Rev. A **22**, 2408 (1980).
[29] D. Vrinceanu and M.R. Flannery, Phys. Rev. Lett. **82**, 3412 (1999).
[30] H. Goldstein, *Classical Mechanics* (Addison-Wesley, Reading, MA, 1980), p. 173.
[31] D. Vrinceanu and M.R. Flannery (unpublished).
[32] *Handbook of Mathematical Functions* edited by M. Abramowitz and I.A. Stegun (Dover Publications, New York, 1972), p. 79.
[33] D. Vrinceanu and M.R. Flannery, J. Phys. B **33**, L721 (2000).
[34] D. Vrinceanu and M.R. Flannery, J. Phys. B **34**, L1 (2001).
[35] J.O. Hirshfelder, J. Phys. Chem. **33**, 1460 (1960).